FINITE ELEMENT ANALYSIS OF MOTOR ECCENTRIC FORCES AND EFFECTS ON VIBRATION

A Dissertation

by

YASHU LI

Submitted to the Office of Graduate and Professional Studies of
Texas A&M University
in partial fulfillment of the requirements for the degree of

DOCTOR OF PHILOSOPHY

Chair of Committee,	Alan Palazzolo
Committee Members,	Steve Suh
	Won-Jong Kim
	Hamid Toliyat
Head of Department,	Andreas A. Polycarpou

May 2019

Major Subject: Mechanical Engineering

ABSTRACT

Machinery trains with motor drives are widely used in industry. Motor related forces may become one of the sources of machinery vibrations. Motor eccentricity is one of the common phenomena that cause forces exerted on motor and the machinery train. The eccentricity between stator and rotor is almost inevitable. Mass unbalance, shaft bending as well as bearing tolerances can introduce the eccentricity. Moreover, modern machines are being designed for higher performance, which often cause significant nonlinear effects. Therefore, a more complete picture of the nonlinear dynamic characteristics brought by motor eccentricity is required to enhance machinery train design, refinement, monitoring and maintenance.

The purpose of the work has been to develop accurate modeling methods of electromagnetic forces, especially at static eccentricity fault, and to study the force effects on driven machinery vibrations. This research work focuses on the characterization of the eccentric forces and their effects of the rotor eccentricity fault on vibration. The most accurate numerical method of finite element method is adopted for field analysis in calculation of characteristics including air gap flux density, eccentric force and torques. An improved movement modeling technique is proposed and developed into the finite element analysis of electric machines.

ACKNOWLEDGEMENTS

I would like to thank my supervising professor Dr. Alan Palazzolo for his guiding my research with knowledge, endeavor and enthusiasm, and his patience, encouragement and invaluable suggestions during the challenging times.

I'd like to thank my committee members, Dr. Steve Suh, Dr. Won-Jong Kim, and Dr. Hamid Toliyat, for their support throughout this research.

I would also like to thank Dr. Xu Han for her early works and assistance. Thanks go to Mr. Erwin Thomas for sharing his knowledge and insights on many problems. Thanks also go to my friends for making my time at College Station a great experience.

Finally, thanks to my parents for their unconditional love and support. Thanks to my fiancé for always being a source of love, encouragement and happiness.

CONTRIBUTORS AND FUNDING SOURCES

Contributors

This work was supervised by a dissertation committee consisting of Dr. Alan Palazzolo and Dr. Steve Suh, Dr. Won-Jong Kim of the Department of Mechanical Engineering and Dr. Hamid Toliyat of the Department of Electrical and Computer Engineering.

The work conducted for the dissertation was completed by the student independently.

Funding Sources

This work is carried out in the Vibrations Controls and Electromechanical Lab (VCEL) at Texas A&M University. It is part of a research project on dynamics and vibration of machinery trains driven by Variable Frequency Drive (VFD) - motors. This work was made possible in part by Turbomachinery Research Consortium (TRC) under Project Number 258124-00089.

TABLE OF CONTENTS

Page

LIST OF FIGURES

Page

LIST OF TABLES

Page

CHAPTER I

INTRODUCTION

Background of Study

Electric machines have been widely used in industry as they can convert electrical energy to mechanical work. Machinery train may experience fault in electric drives which may harm the machinery train performance. Of which the most common one is eccentricity with bearing problems among electric motors. To improve machinery train life and prevent unexpected failure, it's very important to study the machinery train under eccentricity faults. In order to do this, we need first study about the effects of the fault.

Motor Eccentricity

When the rotor of an electric machine is eccentric, the air-gap field between the rotor and the stator becomes uneven, then unwanted vibrations might occur. Motor eccentricity occurs when the stator axis and rotor axis do not coincide. If the rotor axis holds straight, motor eccentricity can be categorized into parallel eccentricity and inclined eccentricity, depending on if rotor axis and stator axis have an angle or not. If the rotor axis has deformation, the motor is in curved eccentricity.

In terms of 2D case, parallel eccentricity is the one of interest. It can further divide into static eccentricity, dynamic eccentricity. The former may result from unintentional misalignment, machining errors/tolerances, thermal distortion etc. The

latter typically results from vibration due to imbalance or other dynamic force producing sources. Figure 1 illustrates the parallel eccentricity. The rotor rotates around its own geometric axis that not in alignment with the stator geometric axis if under static eccentricity fault. For dynamic eccentricity, the rotor is not concentric with the stator either but rotates around the geometric center axis of the stator.

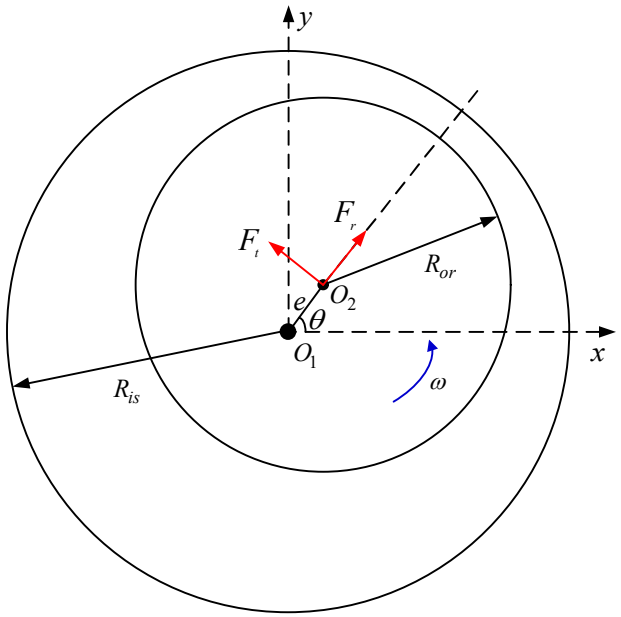

Figure 1 Rotor/stator eccentricity and magnetic radial and tangential forces.

The static eccentricity and dynamic eccentricity may exist at the same time. The combination of the two kinds is called mixed eccentricity. Static eccentricity almost exists in every electric machine, since the rotor axis and stator axis are impossible to perfectly coincide due to assembling or manufacturing errors [1]. Thus the air gaps become unequal that unbalanced magnetic forces (UMFs) [2] might occur on the rotor. Therefore, shafts and bearings may experience excessive stresses. The rotor may then show dynamic eccentricity under the stresses. In worst scenario, rubbing can occur

between the stator and the rotor, and the mechanical part may break. This may cause the machine fail earlier then designed[3].

Eccentricity Force Modeling Methods

In order to understand the eccentric force effects on the system, so that designed machine train can have optimal performance, accurate modeling and computation of the eccentric forces is needed. Many studies have been carried out on eccentricity modeling methods. The approaches can be categorized as the analytical method, the numerical method as well as the hybrid method combining the two.

The analytical methods are adopted widely though a few assumptions are taken. It has the advantage of revealing the origin of the eccentric force. Besides, the simplification due to the assumptions makes problems easier to model and solve. There have been studies focusing on theoretical model of the UMF for different kind of electric machines[4-10] . Finite element methods have been adopted in studies to solve the problem numerically[11-14]. Hybrid methods that combining different methods together to optimize the simulation accuracy and efficiency has been applied as well[15, 16].

Linear model has been taken majority of the studies initially and is found to be accurate enough only for small eccentricity levels[17]. Eccentricity force model that considering the nonlinear property of the magnetic material have been studied more recently [18-22].

Dynamic Behavior of Machines

The magnetic forces may cause serious problems when any component of the forcing frequencies matches one of the machine resonant frequencies. The existence of the eccentricity causes the forces to increase due to the mechanical and magnetic coupling effects. Mechanical system stability that investigated with the effect of eccentric forces are highlighted by studies[1, 6, 12, 18, 22-25].

Significance of Study

Motivation

To study the eccentric force effects on rotordynamics, it's important to have a precise model. Thus, the most accurate method of FEM will be used. Details like slot effects can be considered, which makes it superior to other methods in terms of this research purpose.

Though extensive studies have been done on eccentricity force related research, the majority focused on the electrical indicators of the fault of eccentricity. Usually there is protection between the power supply and the motor drive. In case of harming effects happening, the motor can be cut off from the supply to prevent damage to the motor, but the machinery train is still connected before the motor totally stopped. If unstable effects or large vibration happens at this time, the machinery train may experience harmful forces or torque that causes failure. Therefore, it's important to precisely predict the force effects on vibration.

The work of developing a precise solver for motor eccentricity analysis was initiated first by Dr. Xu Han [24]. The Magnetic Equivalent Circuit (MEC) method was adopted for an induction motor modeling. Due to the sacrifice of accuracy by the MEC method, the author has developed a finite element solver along with applications on different projects.

Objective and Contribution

FEM is to be adopted for mechanical and electromagnetic modeling. A FEM solver is developed aimed at the eccentric force modeling. The FEM solver is capable of geometry building, mesh generation, winding configuration, source option, static and steady-state solution solving, linear and nonlinear material and post-processing. The solver allows for eccentricity modeling and corresponding eccentric force and stiffness results and can be applied to different motor types.

The negative stiffnesses brought by the motor eccentricity may have a harmful effect on the driven machinery train. In the trend of high-performance motor designs, motors with small airgaps may experience more severe effects. Small changes in the airgap flux density may result in great force variation. The influence of the eccentric forces on vibration will be studied with a Jeffcott rotor model.

The most notable scientific contributions of this work are listed below:

(1) Modeling the eccentricity effects of the motor using finite element analysis.

(2) Development of the innovative movement modeling technique connecting the stator and the eccentric rotor.

(3) Calculation of the electromagnetic forces and stiffnesses when the rotor axis is not aligned with the stator axis.

(4) New knowledge of the possible effects of eccentric force harmonics on the electromagnetic forces when the rotor is eccentric.

CHAPTER II

LITERATURE REVIEW ON ELECTROMAGNETIC FORCE CALCULATION

Motor Eccentricity

When motor eccentricity is of interest, most studies investigated induction motors and their air gap are smaller[26]. In [27], authors studied the effects of induction motor pole pairs and rotor slot numbers of line current harmonics under eccentric condition. An adaptive parameter estimation algorithm was proposed in [28] using particle swarm optimization for induction motor mixed eccentricity detection and diagnosis. The effects of static and dynamic eccentricity in induction motor on airgap flux, current and vibration signals were analyzed in [1]. The effects of eccentric force on induction motors were analyzed in [24] and stability analysis was performed on a Jeffcott rotor and an induction motor driven machinery train. The unbalanced magnetic pull caused by the rotor eccentricity in induction motor was studied in [29] with series or parallel winding connections.

Eccentricity in other types includes synchronous machines has been investigated as well. The effects of dynamic airgap eccentricity on inductances of was evaluated for salient pole synchronous machines in [30-32]. Modified winding function method was used. The current harmonics introduced by the rotor eccentricity were studied as well in [32]. In [33], the effect of mixed airgap eccentricity in a salient pole synchronous generator was studied using the same method and formed a diagnosis criteria. Authors in [34] measured the shaft orbit of a salient pole synchronous machine under different load

cases and calculated the iron permeability for calculation of eccentric force using finite element method. Effects of shaft voltages, vibrations and armature currents in a non-salient pole synchronous machine was studied in [35].

Research also has been done in brushless motors with permanent magnets, which are used for small power in automation, hybrid electrical vehicles and robotics and have small air-gap (0.5mm). Static eccentricity effects on the permanent magnet synchronous motor was studied with focus on diagnosis in [36]. The time stepping finite element method was adopted. The same approach was applied in [37] with extension to all three kinds of eccentricity types. Diagnosis of eccentricity types and severity determination was proposed. Kyung-Tae Kim etc. [38] compared the eccentric magnetic forces for interior permanent motors (IPM) and surface mounted permanent magnet (SPM) motors. The IPMs were found to experience higher eccentric forces compared to SPMs under the same level of eccentricity. The permanent magnets in SPMs are usually radially magnetized, thus the produced field can better balance the airgap field caused by eccentricity.

Calculation Methods of Electromagnetic Forces

Accurate modeling of electromagnetic forces is of key importance to investigate their effects on dynamics and vibration. The most common approaches that using analytical method, numerical method or hybrid methods for electromagnetic forces calculations are introduced with their assumptions, advantages and applications in this chapter.

Analytical Method

Popular analytical methods to model the electromagnetic force are listed below in this section. In analytical methods, the permeability of the back iron is usually assumed infinite. In other studies, linear eccentric force models that neglecting the saturation effects are adopted.

Airgap Permeance Method

Analytical methods of using magneto-motive force (MMF) by windings and using air gap permeance method to get air gap field density is extensively used in studies of motor eccentricity. The idea is to use the airgap permeance as a modulation. Thus, the effects of asymmetric air gap caused by motor eccentricity can be taken into consideration.

The common assumptions include infinite permeability of the back iron, which ignores the nonlinearity like saturation and hysteresis. Also, the air gap field is assumed sinusoidally distributed. By this assumption, only the fundamental MMF of air gap is in effect and used. The air gap field is then obtained as the radial field. The tangential flux field is ignored since it's much smaller than the radial contribution [18].

This analytical field solutions can provide good estimates of radial eccentric force only. Other studies have been done to improve the analytical model above to account for both radial and tangential flux density components.

Exact Subdomain Model

Exact subdomain model is another analytical method that shared the idea of FEM that divides the problem domain into several subdomains. Each subdomain is solved, and constraints that ensure smooth connection between them are enforced. Most common subdomains are based on the geometry or material: The stator, the rotor, the airgap, the permanent magnets if present, and the outer boundary domain. This method can allow for electromagnetic force evaluation in both the radial and tangential directions.

Switched reluctance machine exact subdomain model is studied in[39] considering the nonlinearity and saturation of the back iron. Exact subdomain models for the calculation of the magnetic field in open circuit condition of permanent magnet machines is proposed in[40, 41] for different pole and slot combinations. [42] compares different magnetic pole shapes with the proposed ESM model.

Winding Function Approach

The winding function approach provides a way to model the inductance between any two circuits. This method can include all harmonic orders or a few for different modeling accuracy needs.

Much work has been done on the winding function method. [31] proposes the eccentric force for synchronous machines using the winding function method. Faiz[33, 43, 44] has been using the winding function method to model the dynamic eccentricity and extended to other eccentricity types for dynamic simulation as well as fault

detection. Ghoggal[45, 46] uses the modified winding function method to model the eccentric forces for induction motors. [30] uses the winding function method to simulate the eccentric forces for a salient-pole synchronous generator.

Conformal Mapping Method

The method of conformal mapping, also known as conformal transformation is used in deriving air gap permeance to account for the effects of slots and finding the tangential flux density components.

Extensive research has been performed on conformal mapping method. Farhad Rezaee Alam and Karim Abbaszadeh[47] proposes an conformal mapping model for permanent magnet synchronous machines considering all the three kinds of eccentricities. The slot effects, winding configuration and magnetic material saturation effects are also considered. Radial eccentric force effects in permanent magnet synchronous machines are studied in [9].

Magnetic Equivalent Circuit Method

The Magnetic Equivalent Circuit method is also a popular method to analyze the magnetic field of electric machines. The MEC method models the electric machines as a reluctance network.

Unlike analytical methods, MEC can account for important magnetic characteristics like iron nonlinearity such as saturation and hysteresis effects. Relatively accurate results can be obtained depending the MEC network configuration.

Ostovic develops several MEC modeling of induction machines and permanent magnet synchronous machines[48-51]. In[52], an eccentric interior PMSM is studied with eccentric rotor. [53] provides indicators to detect and classify rotor eccentricity levels and demagnetization with the MEC method.

For the above analysis, tangential force was not included. To include eccentric forces in both directions, tangential flux density is needed. To this need, research has been addressed to more complex MEC network. In [24], MEC model was proposed to account for flux density and force in both radial and tangential directions. Saturation effect is considered.

Numerical Method

The most widely used numerical method refers to the Finite Element Method (FEM). The ability of accounting all detailed information such as winding arrangement, teeth shapes, iron material saturation and hysteresis makes the FEM most accurate and reliable method for electric field modeling. It has been widely used in electric machine modeling [54, 55]. FEM was used to calculate the equivalent parameters for induction motors in [56]. In [57], FEM was used for a synchronous motor modeling with iron loss calculated for flywheel application.

[58] investigated the switched-flux permanent magnet motor and [59] studied the squirrel-cage induction motor using FEM. Magnetic field in induction motors are solved using time stepping FEM in [60, 61]. Applications include online current monitoring of the induction motor under static eccentricity fault with discussions of analytical method

limitations and closer agreement with experiment results[62], and static and dynamic eccentricity diagnosis[63]. [38] analyzed the magnetic field distribution with eccentricity to consider the magnetic saturation. But only radial force is considered. Their parametric study of the maximum magnitude of eccentric force has a nonlinear relationship with IPMs.

Hybrid Method

To both have computation efficiency and accuracy, the combination of different method has been investigated with the hybrid method. FEM and boundary element method is combined in [64] to study permanent magnet synchronous machiens. Electromagnetic vibration and acoustics are analyzed. The eddy current loss of an axial flux PM machine is studied in [65] combing the FEM and analytical method.

Eccentric Force Vibration Characteristics

Researches on eccentric force caused vibration are mainly on system stability. In [18], the radial eccentric force was calculated using the air gap permeance method. Maxwell stress tensor method is adopted for the force evaluation. With derived non-dimensional formulation of equations of motion, vibration response was obtained in the complex plane. Stability conditions for synchronous motion was investigated. Their study shows the parameters of electromagnetic stiffness coefficient that used to describe the eccentricity level has a significant effect on the system stability. Frequency response showed a softening effect of the eccentricity forces on the natural frequency and saddle-

node bifurcation zone were found. Jump phenomena were observed. Forces under different load conditions are calculated in [38] using FEM. Stability was found to be affected by the eccentric forces. In [66], radial force in a smooth pole generator was studied depending on rotor positions rather than circular orbits. Finite element beam model was adopted for rotodynamic analysis. Additional harmonic components were found and compared to simplified models indicating the nonlinearity of the eccentric force excitation to the rotor. Jeffcott rotor model is adopted in [24] to evaluate the system stability. Jump phenomena were also observed.

Conclusion

In this chapter, the studies on different types of motors with eccentricity are presented. Calculation methods of eccentric electromagnetic forces are also discussed from the analytical, numerical and comprehensive point of view.

Analytical methods have been widely used due to the computation efficiency and capability of force source and frequency characterization. However, due to the assumption adopted, its accuracy is sacrificed. The numerical results have high accuracy, but the analysis is usually very time consuming when dealing with rotor eccentricity.

In this research, the electromagnetic forces under eccentric fault are studied by numerical method - FEM. This way, the accuracy of the force calculation can be maintained. A novel method of modeling the movement between stator and rotor is proposed. The main advantage of this movement modeling method is that it has no limitations on eccentricity level and no interpolation is needed to maintain good

accuracy. The modeling method of motor with eccentricity is presented and validated, and the force effects on vibration are discussed in the following chapters of this dissertation.

CHAPTER III

FINITE ELEMENT MODELING OF ELECTRIC MACHINES

The basic concept of Finite Element Method (FEM) is to model a problem domain by dividing it into small parts. They are interconnected at points in common to different parts. The solutions for the entire problem domain are then obtained by combining the elements with continuity between elements ensured. The necessary boundary conditions are then imposed.

For this research purpose, FEM provides a way to accurately evaluate the motor eccentricity forces and predict the negative stiffnesses in both the radial and tangential directions. The method allows researchers to comprehensively analyze the effects of motor eccentric forces on vibration. With appropriate assumptions, the three-dimensional electric machines can be simulated with a simplified two-dimensional model. This research focuses on two-dimensional finite element analysis of the electric machines.

An in-house software is developed based on two-dimensional finite element field analysis modeling theory presented in this chapter. Mathematical model is first derived, and then the FEM technique is applied to obtain the FE model. External circuits, movement as well as nonlinearity modeling are included to establish the complete analysis theory. The software is capable of geometry building, mesh generation, solution solving, and post-processing of induction motor and permanent magnet synchronous

motors. Both linear and nonlinear materials are covered. Besides, the software is capable of force and stiffness calculation due to eccentricity.

Mathematical Model and Finite Element Derivation

Maxwell Equations

Electric machines field is considered quasi-static. Thus, the displacement current can be neglected. Thus, the Maxwell's equations for the electromagnetic problem in electrical machines are, in local derivative form:

$$\nabla \boldsymbol{B} = 0 \tag{1}$$

$$\nabla \times \boldsymbol{H} = \boldsymbol{J} \tag{2}$$

$$\nabla \times \boldsymbol{E} = -\frac{\partial \boldsymbol{B}}{\partial t} \tag{3}$$

where $\boldsymbol{B}$ denotes the magnetic flux density, $\boldsymbol{H}$ denotes the magnetic field intensity, $\boldsymbol{J}$ is the electric current density and $\boldsymbol{E}$ denotes the electric field intensity.

The constitutive laws are:

$$\boldsymbol{J} = \sigma(\boldsymbol{E} + \boldsymbol{v} \times \boldsymbol{B}) \tag{4}$$

$$\boldsymbol{B} = \mu_0 \mu_r \boldsymbol{H} \tag{5}$$

where σ is the electrical conductivity, $\boldsymbol{v}$ is the velocity of the material of interest in a given reference frame, μ_0 is the magnetic permeability of free space, and μ_r is the relative permeability.

If a system involves a moving region as electric machines, the last term with velocity in Equation (4) requires special attention. A coordinate system that all the

variables are fixed to the material is adopted. Hence the velocity is always zero in its own coordinate system. The physical explanation behind this technique can be understood from the following respective: the electric field generated by a moving magnetic material in a static magnetic field can be the same as that generated by a constant material in a moving magnetic field. The terms static or moving can be seen in opposite way in different coordinate systems.

Formulation Using the Magnetic Vector Potential

Since the divergence of any curl is zero, the magnetic density can be represented as the curl of a quantity called the magnetic vector potential:

$$\boldsymbol{B} = \nabla \times \boldsymbol{A} \tag{6}$$

Apply Equation (6) in Maxwell's equation in Equation (3), one obtains

$$\nabla \times \boldsymbol{E} + \frac{\partial \boldsymbol{B}}{\partial t} = \nabla \times (\boldsymbol{E} + \frac{\partial \boldsymbol{A}}{\partial t}) = 0 \tag{7}$$

With Equation (7) , the electric scalar potential $\boldsymbol{\Phi}$ can be introduced

$$\boldsymbol{E} + \frac{\partial \boldsymbol{A}}{\partial t} = -\nabla \boldsymbol{\Phi} \tag{8}$$

With Equation (8), the current density with respect to a fixed-to-material frame can be written as

$$\boldsymbol{J} = \sigma \boldsymbol{E} = \sigma \left(-\frac{\partial \boldsymbol{A}}{\partial t} - \nabla \boldsymbol{\Phi} \right) \tag{9}$$

Replacing Equation (5) and (9) in (2), we have

$$\nabla \times (\frac{1}{\mu_0 \mu_r} \nabla \times \boldsymbol{A}) = \sigma(-\frac{\partial \boldsymbol{A}}{\partial t} - \nabla \Phi) \tag{10}$$

Given the assumptions of 2D analysis, the magnetic induction is defined only in the Oxy plane. Therefore, the problem can be reduced to scaler form: The magnetic vector potential $\boldsymbol{A} = A\boldsymbol{k}$ and the current density $\boldsymbol{J} = J\boldsymbol{k}$ have only one component, where $\boldsymbol{k}$ is the unit vector in the z direction.

Thus in 2D analysis, Equation (10) can be written as

$$\frac{1}{\mu_0 \mu_r} \nabla^2 A = \sigma \left(\frac{\partial A}{\partial t} + \nabla \Phi \right) \tag{11}$$

Formulation of the Finite Element Equations

In finite element method, the following formula is used to approximate the solution:

$$A(x, y, t) = \sum_{e=1}^{N_e} \sum_{i=1}^{3} A_{ei}(t) N_{ei}(x, y) \tag{12}$$

where $A_{ei}(t)$ is the magnetic vector potential of the i^{th} node in e^{th} element, and N_{ei} is the corresponding shape function.

First-order triangle elements are used due to simple formulation and high calculation efficiency. The shape function defined on e^{th} element Ω_e has the form

$$N_{ei}(x, y) = \frac{1}{2\Delta_e} \left(p_i + q_i x + r_i y \right) \tag{13}$$

and $N_{ei}(x, y) = 0$ everywhere else. Δ_e denotes the area of the e^{th} element, $i = 1, 2, \text{or } 3$.

With (ei, ej, ek) be the cyclic permutations of $(e1, e2, e3)$, the coefficients are defined as

$$\begin{aligned} p_{ei} &= x_{ej} y_{ek} - x_{ek} y_{ej} \\ q_{ei} &= y_{ej} - y_{ek} \\ r_{ei} &= x_{ek} - x_{ej} \end{aligned} \tag{14}$$

For the linear shape function,

$$N_i(x_j, y_j) = \begin{cases} 1, & i = j \\ 0, & i \neq j \\ 0, & \text{otherwise} \end{cases} \tag{15}$$

Consideration of Boundary Conditions

Boundary conditions need to be defined to close the problem. The specification of unknowns is called the Dirichlet boundary conditions. And the specification of gradients or derivatives of the unknowns on the boundary is called the Neumann boundary conditions. In the setup of the 2D finite element solver, the boundary is the outer and inner boundary of the cross-section of the machine. If magnetic fields are constrained inside this boundary, we enforce the Homogeneous Dirichlet boundary condition on the boundary, that is:

$$A^{\Gamma_1} = 0 \tag{16}$$

where Γ_1 is the prescribed boundary.

Besides the essential boundary condition shown in Equation (16), the homogeneous Neumann boundary condition is also automatically satisfied.

Galerkin Discretization

The Galerkin approach is adopted that the weight function takes the same form as the shape function. The residual function R_Ω is defined on the domain as

$$R_\Omega = \frac{1}{\mu_0 \mu_r} \nabla^2 A - \sigma \left(\frac{\partial A}{\partial t} + \nabla \Phi \right) \tag{17}$$

The following equation needs to be satisfied:

$$\int_\Omega w R_\Omega \mathrm{d}\Omega = 0 \tag{18}$$

That is,

$$\int_\Omega w \left(\frac{1}{\mu_0 \mu_r} \nabla^2 A - \sigma \left(\frac{\partial A}{\partial t} + \nabla \Phi \right) \right) \mathrm{d}\Omega = 0 \tag{19}$$

Apply weak form to the first term,

$$\begin{aligned} \int_\Omega w \nabla^2 A \mathrm{d}\Omega &= -\int_\Omega \nabla w \nabla A \mathrm{d}\Omega + \oint_\Gamma w \nabla A \mathrm{d}\Gamma \\ &= -\int_\Omega \nabla w \nabla A \mathrm{d}\Omega + \oint_\Gamma w \frac{\partial A}{\partial n} \mathrm{d}\Gamma \end{aligned} \tag{20}$$

The boundary integral term in Equation (20) is set to zero, which implies the homogeneous Neumann boundary.

Thus Equation (19) can be written as

$$\int_\Omega \left(\frac{1}{\mu_0 \mu_r} \nabla w \nabla A + w \sigma \frac{\partial A}{\partial t} - w \sigma \nabla \Phi \right) \mathrm{d}\Omega = 0 \tag{21}$$

To find the solutions $A_{ei}(t)$ on the nodes to satisfy Equation (21), the approximated form as shown in Equation (12) is used.

Formulation of Matrix Equations

First, consider electric machines without permanent magnets. The term $\sigma\nabla\Phi$ only appears in the stator windings and can be written as forced current density J_f if the electric machine is current excited. Apply the solution form in Equation (12) and weight function as the same form as shape function to Equation (21), for the e^{th} element:

$$\sum_{i=1}^{3}\int_{\Omega_e}\nu A_{ei}(t)\nabla N_{ei}\nabla N_{ej}+\sigma\frac{\mathrm{d}A_{ei}(t)}{\mathrm{d}t}N_{ei}N_{ej}\mathrm{d}\Omega-\int_{\Omega_e}N_{ei}J_f\mathrm{d}\Omega=0 \tag{22}$$

where $\nu=\dfrac{1}{\mu_0\mu_r}$, the reluctivity, is used for convenience.

Write the equation in matrix form,

$$\boldsymbol{D}_e\frac{\mathrm{d}}{\mathrm{d}t}\boldsymbol{A}_e(t)+\boldsymbol{K}_e\boldsymbol{A}_e(t)=\boldsymbol{J}_e \tag{23}$$

where

$$D_{ij}=\int_{\Omega_e}\sigma N_iN_j\mathrm{d}\Omega \tag{24}$$

$$K_{ij}=\frac{1}{\mu_0\mu_r}\int_{\Omega_e}\nabla N_i\nabla N_j\mathrm{d}\Omega \tag{25}$$

$$J_i=\int_{\Omega_e}N_iJ_f\mathrm{d}\Omega \tag{26}$$

The divergence of the shape function as shown in Equation (22) and (25) is

$$\nabla N_{ei}(x_j,y_j)=\boldsymbol{i}\frac{q_{ei}}{2\Delta_e}+\boldsymbol{j}\frac{r_{ei}}{2\Delta_e} \tag{27}$$

and $\nabla N_{ei}(x,y)=0$ everywhere else.

Thus,

$$D_{ij} = \begin{cases} \dfrac{\sigma\Delta_e}{6}, & i = j \\ \dfrac{\sigma\Delta_e}{12}, & i \neq j \end{cases} \tag{28}$$

That is,

$$\boldsymbol{D}_e = \frac{\sigma\Delta_e}{12}\begin{bmatrix} 2 & 1 & 1 \\ 1 & 2 & 1 \\ 1 & 1 & 2 \end{bmatrix} \tag{29}$$

The stiffness matrix can be determined by

$$\begin{aligned} K_{ij} &= \frac{1}{\mu_0\mu_r}\int_{\Omega_e}\left(\boldsymbol{i}\frac{q_{ei}}{2\Delta_e} + \boldsymbol{j}\frac{r_{ei}}{2\Delta_e}\right)\left(\boldsymbol{i}\frac{q_{ej}}{2\Delta_e} + \boldsymbol{j}\frac{r_{ej}}{2\Delta_e}\right)\mathrm{d}\Omega \\ &= \frac{1}{4\mu_0\mu_r\Delta_e}\left(q_{ei}q_{ej} + r_{ei}r_{ej}\right) \end{aligned} \tag{30}$$

The source current is obtained by

$$J_i = \int_{\Omega_e} N_i J_f \mathrm{d}\Omega = \frac{\Delta_e}{3} J_f \tag{31}$$

Voltage Source

The voltage equation for the coil can be written as

$$U = RI + \frac{\mathrm{d}}{\mathrm{d}t} n\phi \tag{32}$$

where U is the voltage applied on the coil, R is the resistance, I is the current flows in the coil, n is the turns density, and ϕ is the flux linkage linked by the coil.

As presented in previous sections, the current contribution of an element is given by

$$\boldsymbol{J} = \frac{J\Delta_e}{3}\begin{bmatrix}1\\1\\1\end{bmatrix} = \frac{N\Delta_e}{3\sum\Delta_e}\begin{bmatrix}1\\1\\1\end{bmatrix} I = \boldsymbol{P}I \tag{33}$$

where N is the total number of turns and $\sum\Delta_e$ is the total area.

From the Gauss's law and Stokes theorem, the flux, in terms of the magnetic vector potential in 2D case, is given by

$$\phi = l\left(A_1 - A_2\right) \tag{34}$$

If the reference magnetic potential is taken zero, it can further be simplified as

$$\phi = lA \tag{35}$$

Define the coil turn density as the ratio of turns over coil area

$$\kappa = \frac{N}{\sum\Delta_e} = \frac{n}{\Delta_e} \tag{36}$$

where n denotes the number of turns within the specific element.

The flux linkage can be represented by

$$n\phi = \frac{\kappa\Delta_e l}{3}(A_1 + A_2 + A_3) = \frac{\kappa\Delta_e l}{3}\begin{bmatrix}1\\1\\1\end{bmatrix}^T \boldsymbol{A} = \boldsymbol{Q}\boldsymbol{A} \tag{37}$$

Thus, the system equations involve the field is

$$\boldsymbol{K}\boldsymbol{A} = \boldsymbol{P}\boldsymbol{I} \tag{38}$$

And the coil with voltage source equation is

$$\boldsymbol{Q}\frac{\mathrm{d}}{\mathrm{d}t}\boldsymbol{A} + \boldsymbol{R}\boldsymbol{I}(t) = \boldsymbol{U}(t) \tag{39}$$

FEM Coupling with Electric Circuit

The modeling of finite element model coupled to external electric circuits will be presented in this section. The conductors in electric machines are presented as electric circuit model. Take the induction motor as example, there are two types of conductors: the stator winding and the rotor bars.

The solid rotor bars are where eddy currents cannot be neglected. The stator winding is referred as thin conductors where skin effect can be neglected.

Rotor Bar Electric Circuit Model

Consider a solid bar with cross-section area of S_t and length of l . The d.c. resistance of the bar would be

$$R_t = \frac{l}{\sigma S_t} \tag{40}$$

The voltage drop over the rotor bar U_t is

$$U_t = R_t I_t + R_t \int_{S_t} \sigma \frac{\partial A}{\partial t} \mathrm{d}s \tag{41}$$

where I_t is the current in the rotor bars.

The voltage drop on the rotor bar can also be represented as the integral of the gradient of the scalar electric potential:

$$U_t = \int_0^l -(\nabla \Phi) \mathrm{d}l \tag{42}$$

Thus for the system with the rotor bar, apply Equation (42) into the system equation (11), the governing equation then has the form of

$$\frac{1}{\mu_0 \mu_r} \nabla^2 A - \sigma \frac{\partial A}{\partial t} + \sigma \frac{U_t}{l} = 0 \tag{43}$$

Stator Winding Electric Circuit Model

Consider a coil with N_{co} turns that are serial connected. It has cross section s_f and length l_f, thus the total surface area of the coil would be $S_f = N_{co} s_f$. Denote the current following in the winding as I_f.

Apply Equation (41) in Equation (43), and replace I_t with I_f for coils,

$$\frac{1}{\mu_0 \mu_r} \nabla^2 A - \sigma \frac{\partial A}{\partial t} + \sigma \frac{R_f I_f + R_f \int_{s_f} \frac{\partial A}{\partial t} \mathrm{d}s}{l_f} = 0 \tag{44}$$

Similarly, the d.c. resistance $R_f = \frac{l_f}{\sigma s_f}$ in coils.

Since the induced current density is uniform in coils, the second and fourth items cancel with each other in Equation (44), it reduces to

$$\frac{1}{\mu_0 \mu_r} \nabla^2 A + \frac{N_{co}}{S_f} I_f = 0 \tag{45}$$

Thus, the winding's voltage and current:

$$U_f = R_f I_f + \frac{N_{co} l_f}{S_f} \int_{S_f} \frac{\partial A}{\partial t} \mathrm{d}s \tag{46}$$

Coupled Finite Element and Electric Model

According to the above presented theory for magnetic material, rotor bars and windings, the equations for the induction motor are

$$\frac{1}{\mu_0 \mu_r} \nabla^2 A - \sigma \frac{\partial A}{\partial t} + \frac{N_{co}}{S_f} I_f + \sigma \frac{U_t}{l} = 0 \tag{47}$$

$$U_t = R_t I_t + R_t \int_{S_t} \sigma \frac{\partial A}{\partial t} \mathrm{d}s \tag{48}$$

$$U_f = R_f I_f + L \frac{\mathrm{d}}{\mathrm{d}t} I_f + \frac{N_{co} l_f}{S_f} \int_{S_f} \frac{\partial A}{\partial t} \mathrm{d}s \tag{49}$$

In Equation (49), L is introduced to consider the end winding effects.

Apply the Galerkin method to Equations (47)-(49), the equations in matrix form are

$$\boldsymbol{K}\boldsymbol{A} + \boldsymbol{D} \frac{\mathrm{d}}{\mathrm{d}t} \boldsymbol{A} - \boldsymbol{P}\boldsymbol{I}_f - \boldsymbol{P}' \boldsymbol{U}_t = \boldsymbol{J} \tag{50}$$

$$\boldsymbol{Q}' \frac{\mathrm{d}}{\mathrm{d}t} \boldsymbol{A} + \boldsymbol{R}' \boldsymbol{I}_t = \boldsymbol{U}_t \tag{51}$$

$$\boldsymbol{Q} \frac{\mathrm{d}}{\mathrm{d}t} \boldsymbol{A} + \boldsymbol{R}\boldsymbol{I}_f + \boldsymbol{L} \frac{\mathrm{d}}{\mathrm{d}t} \boldsymbol{I}_f = \boldsymbol{U}_f \tag{52}$$

The vectors $\boldsymbol{I}_f$, $\boldsymbol{U}_f$, and $\boldsymbol{I}_t$, $\boldsymbol{U}_t$ are currents and voltages of the windings and rotor bars respectively. $\boldsymbol{R}$ and $\boldsymbol{R}'$ are the d.c. resistance matrix of the windings and rotor bars respectively. And $\boldsymbol{L}$ is the diagonal matrix of the end-windings inductances. Other matrices terms are

$$P_{ij} = \int_S \frac{N_{coj}}{S_{fj}} N_i \mathrm{d}s \tag{53}$$

if node i belongs to the winding j region, or zeros everywhere else.

$$P'_{ij} = \int_S \frac{\sigma_j}{l} N_i \mathrm{d}s \tag{54}$$

if node i belongs to the rotor bar j region, or zeros everywhere else.

$$Q_{ij} = \int_S \frac{N_{coi} l}{S_{fi}} N_j \mathrm{d}s \tag{55}$$

if node i belongs to the winding j region, or zeros everywhere else.

$$Q'_{ij} = \int_S \frac{l}{S_{ti}} N_j \mathrm{d}s \tag{56}$$

if node i belongs to the rotor bar j region, or zeros everywhere else.

Discretization of Time Derivative

Time discretization method is adopted to solve the differential equations. Popular discretization of time derivatives can be obtained by the back Euler's algorithm or the Crank-Nicholson algorithm.

Mechanical Movement

To enable the dynamic behavior to be modelled, or to consider the losses and forces such as ripple torque arising from magneto-motive force and permeance harmonics, movement must be incorporated in the finite element model for machine analysis. The most intuitive method is to re-mesh the region. But this will harm the efficiency and has a higher memory requirement.

The existing movement models can be divided into two categories: those which construct a special “band” in the air-gap, and those which model the air-gap region with techniques that more conveniently deal with relative motion.

The methods introduced here rely upon a moving band technique. Meshes are divided into the stationary part fixed to the stator and the moving part fixed to the rotor. The meshes are solved in their own frames. The continuity between them are ensured. As stated earlier, velocity term can be omitted based on this choice of coordinate system. There is no source present in the air gap region. This approach is called a pseudo static formulation.

Time-stepping Technique

The time-stepping technique was adopted in the code for the concentric motor and constant speed cases.

The time-stepping method creates a moving surface in the air-gap between stator and rotor. The surface is subdivided into several equal intervals whose length corresponds to the length of the time step so that as the rotor moves, nodes on the moving surface always coincide peripherally.

It’s easy to implement the method if the rotation speed is constant. It is also suitable for the computation of forces. But this method does not allow eccentric movement.

Novel Moving-band Technique

To satisfy the needs of study of the force and negative stiffness due to motor eccentricity and enhance the extendibility of the software (e.g. non-constant speed), new movement modeling method is needed.

As stated above, “re-mesh” is inevitable because of the rotation especially in eccentric cases. Automatic re-mesh with the setting of Delaunay triangle sizes and aspect ratios only may change the nodes numbers and make the problem harder to get to a converged solution.

The proposed method for movement modeling as used in the solver is to keep the number of nodes constant during each rotor position while re-connect the nodes in the air gap region only to update the connectivity matrix.

To maintain the number of the nodes constant, the stationary part and the rotating part are meshed separately with all the nodes and meshes information saved. Both stationary and rotating region contain the back iron, the slots and slot openings. Special care only needs to be paid to the remaining airgap ring region.

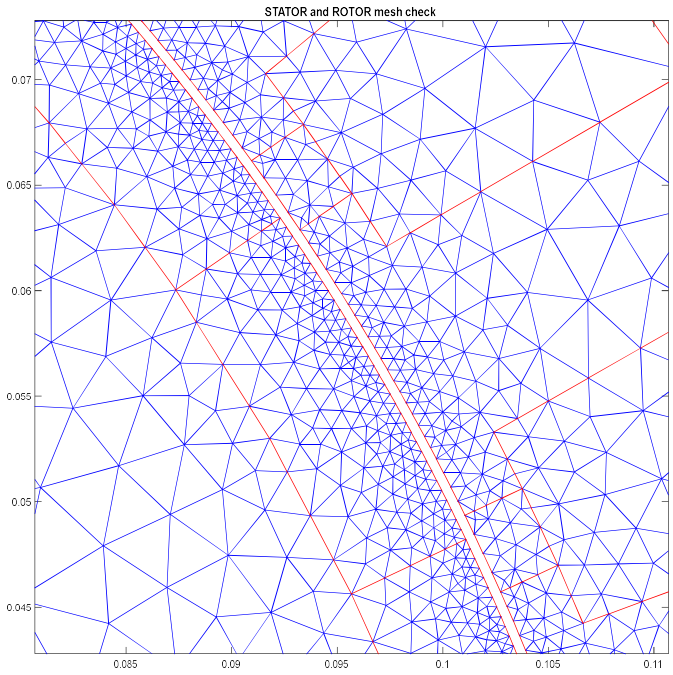

Figure 2 Mesh of an electric machine without airgap ring region

The nodes on the airgap ring boundary are used as key points for the airgap ring mesh. Key nodes denote that the nodes on the airgap ring from the stationary and rotating region mesh are the only ones for the mesh inside the airgap ring. One or more layers of nodes will be inserted in the air gap depending on the slot shape, slot opening size, airgap length and eccentricity. Meshes are formed within the airgap ring and the nodes on the stator or rotor boundaries.

Figure 3 shows a 2-layer mesh detail of the airgap, indicating the moving band region in connection of the stator side and the rotor side.

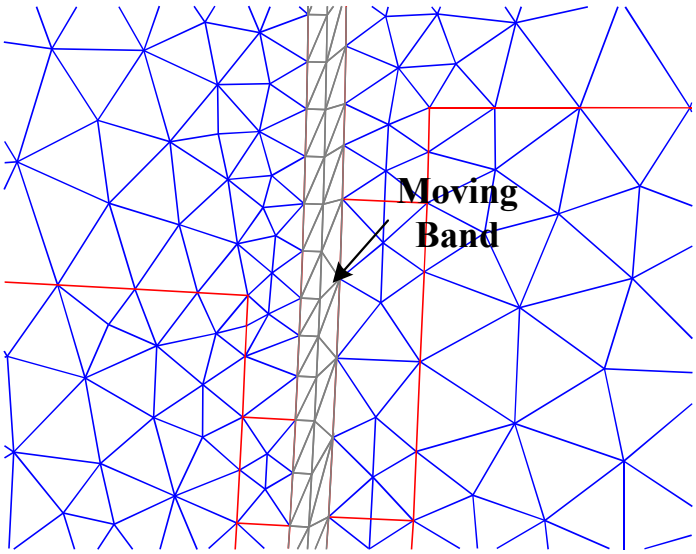

Figure 3 Airgap ring mesh for moving band technique

The number of the nodes on the inner and outside boundary need to be compared. The one with more nodes is called the master boundary and the other called slave boundary. The nodes on the master boundary are then mapped radially on all the inserted layers. Connect the nodes to form the mesh and the connectivity matrix. All meshes are kept except for the layer closest to the rotating part.

The mesh and connectivity matrix of the layer closest to the rotating part needs to be updated through reconnection at each rotor position. This can be done by shifting the connectivity matrix connecting nodes in the reverse rotating direction or by re-mesh to form new connectivity matrix. While the number of nodes is kept constant, the mesh size of the problem may vary as the rotor rotates.

Procedures to realize the above method are summarized as below:

(1) Auto mesh the motor stator and rotor separately with airgap slots to obtain the key points on the airgap boundary. The key points are to be used for air gap ring mesh.

(2) Calculate the number of the key points on airgap ring. The side with more nodes is noted as master boundary, and the other slave boundary.

(3) Add one or more layers in the center of the airgap ring. Map all the master boundary nodes on the middle layers and the slave boundary. Create meshes.

(4) Match all the mapped nodes on the slave boundary to the original slave nodes.

(5) Fix Inserted middle layers nodes location and update the mesh. If master side rotates, update the connection of the master side. A simple rotation matrix will do the work. If slave side rotates, match the mapped nodes on the slave boundary (always at initial location) with current slave boundary nodes and then repeat step (4).

This method saves the computation time in an appreciable way. Besides, no model size changing, or interpolation is needed since nodes are kept constant. The above method also provides the capability of modeling various configuration of rotor and stator slot number and slot shapes.

Nonlinearity

Motor back iron usually uses the nonlinear material. Since each element can experience a different field, the permeability of each element can be determined based

on the BH curve. The chord method[67] is applied here to minimize oscillation until its convergence,

$$\nu_{e,i+1} = \nu_{e,i} + \alpha(\nu^*_{e,i} - \nu_{e,i}) \tag{57}$$

for e^{th} element and $(i+1)^{\text{th}}$ iteration. α is the acceleration constant and $\nu^*_{e,i}$ is the calculated reluctivity from the i^{th} iteration.

The convergence requirements are set to be:

$$\sqrt{\frac{\sum_{e=1}^{N_e} \left| B_{e,i} - B_{e,i-1} \right|^2}{\sum_{e=1}^{N_e} B_{e,i}^2}} \le \varepsilon_B \tag{58}$$

where N_e is the total element number and $B_{e,i}$ is the flux density of e^{th} element for the i^{th} iteration.

$$\sqrt{\frac{\sum_{n=1}^{N_p} \left| A_{n,i} - A_{n,i-1} \right|^2}{\sum_{e=1}^{N_p} A_{n,i}^2}} \le \varepsilon_A \tag{59}$$

where N_p is the total node number and $A_{n,i}$ is the magnetic potential of n^{th} node for the i^{th} iteration.

Direct Iteration

For nonlinear problems, direction iteration approach is in common use for simple application and robustness for convergence. Following is the flow chart for the direct iteration approach considering the nonlinearity.

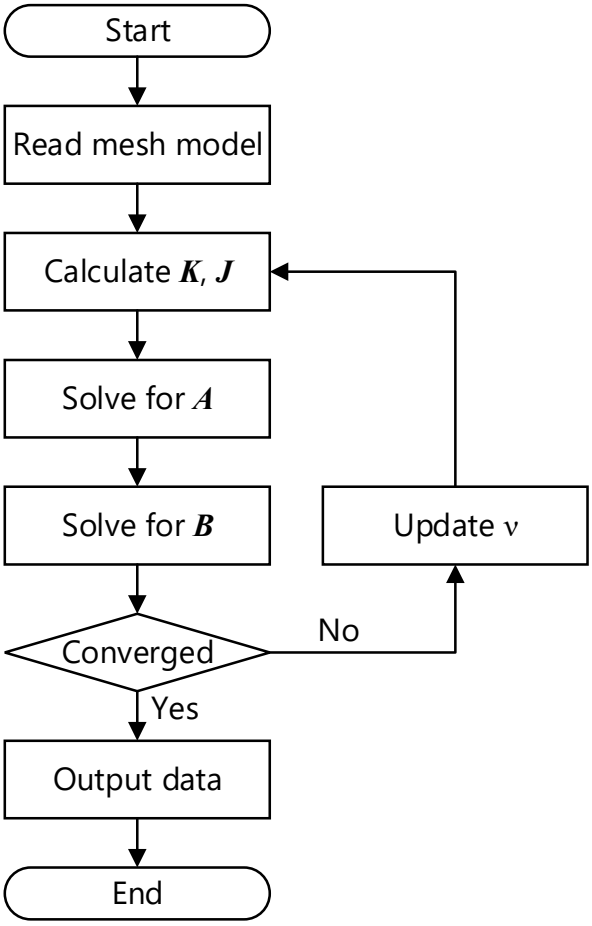

Figure 4 Flowchart for Nonlinear Finite Element Solution

Newton Method

An obvious drawback of the direct iteration method is that the pace to get convergence is slow. The Newton iteration procedure then can be used to expedite the process, since the solution is searched by tangent functions of the B-H curve instead of the linear search. The incremental solution vector $\Delta \boldsymbol{A}$ can be obtained from

$$\Delta \boldsymbol{A} = -\hat{\boldsymbol{T}}^{-1}(\boldsymbol{A}_{s+1}^{r})\boldsymbol{R}_{s+1}^{r} \tag{60}$$

where $\hat{\boldsymbol{T}}$ is the tangent matrix given by

$$\hat{\boldsymbol{T}}(\boldsymbol{A}_{s+1}^{r}) \equiv \left(\frac{\partial \boldsymbol{R}_{s+1}}{\partial \boldsymbol{A}_{s+1}} \right)^{r}, \quad \boldsymbol{R}_{s+1}^{r} = \hat{\boldsymbol{K}}(\boldsymbol{A}_{s+1}^{r})\boldsymbol{A}_{s+1}^{r} - \hat{\boldsymbol{F}} \tag{61}$$

where $\boldsymbol{R}_{s+1}^{r}$ denotes the residual vector at $(s+1)$ time step with r-th iteration.

The total solution can be obtained as

$$\boldsymbol{A}_{s+1}^{r+1} = \boldsymbol{A}_{s+1}^{r} + \Delta \boldsymbol{A} \tag{62}$$

Eccentric Force Calculation

Magnetic Flux Density

After the magnetic flux potential is obtained, the magnetic flux density can be achieved from (6) in 2D case:

$$B_{ex} = \frac{\partial A}{\partial y} = \frac{1}{2\Delta_e} \sum_{i=1}^{3} r_i A_i \tag{63}$$

$$B_{ey} = -\frac{\partial A}{\partial x} = -\frac{1}{2\Delta_e} \sum_{i=1}^{3} q_i A_i \tag{64}$$

Force Calculation

With the fields known, the calculation of forces through Maxwell stress tensor is used extensively in computer programs and is applied in the software.

The Maxwell stresses are determined from the radial and tangential flux density components as, respectively

$$\sigma_t = \frac{B_r B_t}{\mu_0} \tag{65}$$

$$\sigma_r = \frac{B_r^2 - B_t^2}{2\mu_0} \tag{66}$$

The tangential incremental force is given by

$$\mathrm{d}F_t = \sigma_t \mathrm{d}l \tag{67}$$

The normal component is

$$\mathrm{d}F_r = \sigma_r \mathrm{d}l \tag{68}$$

The eccentric forces in x and y directions are calculated with the Maxwell stress tensor as:

$$F_x = rl \int_0^{2\pi} \left(\sigma_r \cos\theta - \sigma_t \sin\theta\right) \mathrm{d}\theta \tag{69}$$

$$F_y = rl \int_0^{2\pi} \left(\sigma_r \sin\theta + \sigma_t \cos\theta\right) \mathrm{d}\theta \tag{70}$$

where r is the integration path radius and l is the depth of the fields in the electric machine for the 2D model.

Negative Stiffness Calculation

The negative stiffness is calculated by the change of force divided by the change of eccentricity.

Negative stiffness of *x*-direction due to eccentricity

$$K_{xx} = -\frac{\Delta F_x}{e} \tag{71}$$

Negative cross coupled stiffness of y-direction due to eccentricity

$$K_{yx} = -\frac{\Delta F_y}{e} \tag{72}$$

CHAPTER IV

ECCENTRIC FORCE CHARACTERISTICS OF INDUCTION MOTOR

Different connections of rotor bars and stator windings can be found in electrical devices. The most common squirrel-cage induction motor is taken as an example to illustrate the configuration.

Squirrel-Cage Induction Motor Formulation

In the squirrel-cage induction motor model, rotor bars are parallel connected and short-circuited, while the stator windings are independently fed by an external voltage source. The star connection of windings without neutral is studied here.

Equations for Parallel Connected and Short-circuited Rotor Bars

The parallel-connected rotor bars as in the case of squirrel-cage induction motors are shown as in. The rotor bars are short circuited by end windings with resistance r_{er} and inductance l_{er}.

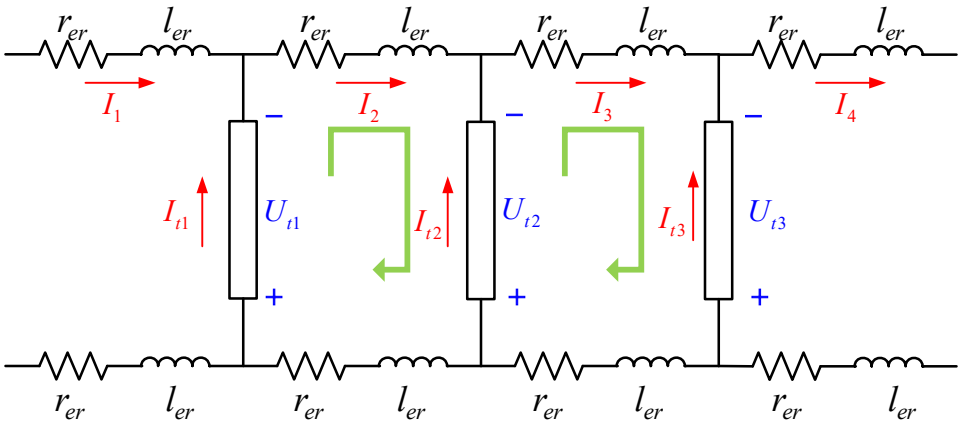

Figure 5 Squirrel-cage Type Rotor Connection

For Loop 1, according to Kirchhoff's Voltage Law,

$$2r_{er}I_2 + 2l_{er}\frac{\mathrm{d}}{\mathrm{d}t}I_2 - U_{t2} + U_{t1} = 0 \tag{73}$$

Write (73) in matrix form, considering all the N_{rb} rotor bars:

$$\boldsymbol{R}_{er}\boldsymbol{I} + \boldsymbol{L}_{er}\frac{\mathrm{d}}{\mathrm{d}t}\boldsymbol{I} + \boldsymbol{C}_{rb}\boldsymbol{U}_t = \boldsymbol{0} \tag{74}$$

where the end winding resistance matrix has the form

$$\boldsymbol{R}_{er} = \begin{bmatrix} 2r_{er} & & & \\ & 2r_{er} & & \\ & & \ddots & \\ & & & 2r_{er} \end{bmatrix} \tag{75}$$

The end winding inductance matrix has the form

$$\boldsymbol{L}_{er} = \begin{bmatrix} 2l_{er} & & & \\ & 2l_{er} & & \\ & & \ddots & \\ & & & 2l_{er} \end{bmatrix} \tag{76}$$

The rotor bar coefficient matrix is

$$\boldsymbol{C}_{rb}=\begin{bmatrix}-1 & 0 & \cdots & 1\\ 0 & -1 & \cdots & 0\\ \vdots & \vdots & \ddots & \vdots\\ 0 & 0 & \cdots & -1\end{bmatrix} \tag{77}$$

The ending winding current vector $\boldsymbol{I}$ are related to the vector of rotor bar currents $\boldsymbol{I}_t$ by

$$\boldsymbol{I}_t=\begin{bmatrix}I_{t1}\\ I_{t2}\\ \vdots\\ I_{tN_{rb}}\end{bmatrix}=\begin{bmatrix}-1 & 0 & \cdots & 0\\ 0 & -1 & \cdots & 0\\ \vdots & \vdots & \ddots & \vdots\\ 1 & 0 & \cdots & -1\end{bmatrix}\begin{bmatrix}I_1\\ I_2\\ \vdots\\ I_{N_{rb}}\end{bmatrix}=\boldsymbol{C}_{rb}^{\mathrm{T}}\boldsymbol{I} \tag{78}$$

where superscript ^{T} denote a transposed matrix.

Thus, the voltage and current of rotor bars are related by

$$\boldsymbol{R}_{er}\boldsymbol{I}_t+\boldsymbol{L}_{er}\frac{\mathrm{d}}{\mathrm{d}t}\boldsymbol{I}_t+\boldsymbol{C}_{rb}^{\mathrm{T}}\boldsymbol{C}_{rb}\boldsymbol{U}_t=\boldsymbol{0} \tag{79}$$

Hence rotor bar related equations are

$$\begin{aligned}\boldsymbol{Q}'\frac{\mathrm{d}}{\mathrm{d}t}\boldsymbol{A}+\boldsymbol{F}_{Ut}\boldsymbol{U}_t+\boldsymbol{R}'\boldsymbol{I}_t&=\boldsymbol{0}\\ \boldsymbol{C}_{rb}^{\mathrm{T}}\boldsymbol{C}_{rb}\boldsymbol{U}_t+\boldsymbol{R}_{er}\boldsymbol{I}_t+\boldsymbol{L}_{er}\frac{\mathrm{d}}{\mathrm{d}t}\boldsymbol{I}_t&=\boldsymbol{0}\end{aligned} \tag{80}$$

Where $\boldsymbol{F}_{Ut}$ is the negative identity matrix $\boldsymbol{F}_{Ut}=$ -eye(N_{rb}).

Equations for Star Connected Windings without Neutral

$N_w - 1$ linearly independent variables exist for a star connected N_w windings. I some other cases, the windings can be fed by a set of poly-phase sources. Consider the case of N_p phase source, there are only $N_p - 1$ linearly independent variables.

Let $\boldsymbol{I}_f^*$ denote the linearly independent winding currents, thus

$$\boldsymbol{I}_f = \boldsymbol{F}_w \boldsymbol{I}_f^* \tag{81}$$

where $\boldsymbol{F}_w$ is an illustration of winding function and takes the form of $\boldsymbol{F}_{rb}$ in dimension of $N_w \times (N_w - 1)$.

Thus, the equation for the winding is

$$\boldsymbol{F}_w^{\mathrm{T}} \boldsymbol{Q} \frac{\mathrm{d}}{\mathrm{d}t} \boldsymbol{A} + \boldsymbol{F}_w^{\mathrm{T}} \boldsymbol{R} \boldsymbol{F}_w \boldsymbol{I}_f^* + \boldsymbol{F}_w^{\mathrm{T}} \boldsymbol{L} \boldsymbol{F}_w \frac{\mathrm{d}}{\mathrm{d}t} \boldsymbol{I}_f^* = \boldsymbol{F}_w^{\mathrm{T}} \boldsymbol{U}_f \tag{82}$$

Equations for the Whole Domain

The matrix system describing the squirrel-cage type induction motor with star type winding without neutral can be obtained as:

$$\begin{aligned}
&\boldsymbol{K}\boldsymbol{A} + \boldsymbol{D} \frac{\mathrm{d}}{\mathrm{d}t} \boldsymbol{A} - \boldsymbol{P} \boldsymbol{F}_w \boldsymbol{I}_f^* - \boldsymbol{P}' \boldsymbol{U}_t = \boldsymbol{0} \\
&\boldsymbol{Q}' \frac{\mathrm{d}}{\mathrm{d}t} \boldsymbol{A} + \boldsymbol{F}_{Ut} \boldsymbol{U}_t + \boldsymbol{R}' \boldsymbol{I}_t = \boldsymbol{0} \\
&\boldsymbol{C}_{rb}^{\mathrm{T}} \boldsymbol{C}_{rb} \boldsymbol{U}_t + \boldsymbol{R}_{er} \boldsymbol{I}_t + \boldsymbol{L}_{er} \frac{\mathrm{d}}{\mathrm{d}t} \boldsymbol{I}_t = \boldsymbol{0} \\
&\boldsymbol{F}_w^{\mathrm{T}} \boldsymbol{Q} \frac{\mathrm{d}}{\mathrm{d}t} \boldsymbol{A} + \boldsymbol{F}_w^{\mathrm{T}} \boldsymbol{R} \boldsymbol{F}_w \boldsymbol{I}_f^* + \boldsymbol{F}_w^{\mathrm{T}} \boldsymbol{L} \boldsymbol{F}_w \frac{\mathrm{d}}{\mathrm{d}t} \boldsymbol{I}_f^* = \boldsymbol{F}_w^{\mathrm{T}} \boldsymbol{U}_f
\end{aligned} \tag{83}$$

Example Motor Geometry and Input Parameters

The same 3-phase induction motor example as presented in [68] with eccentricity fed by three-phase rated voltage is simulated here for model validation as well as comparison of the finite element method and the magnetic equivalent circuit method. This is a squirrel cage type. Figure 6 shows the model that generated by the in-house software and the color denotes different phase of windings.

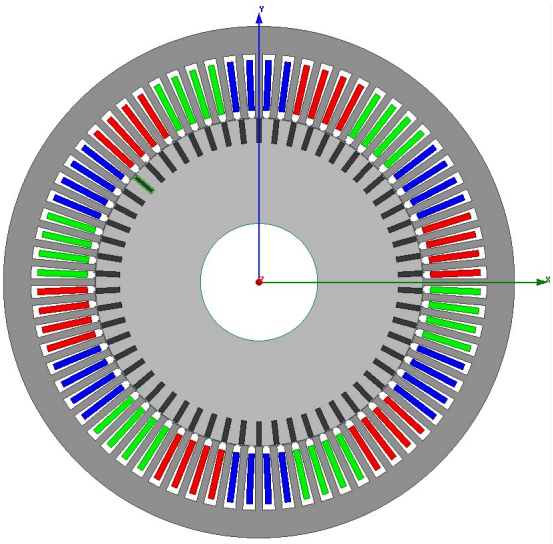

Figure 6 Example Induction Motor Model

The general information of the induction motor is listed in Table 1. The stator winding connections are formed by single layer full pitch connection.

Table 1 Example Induction General Information

General Information	
Rated Output Power (kW)	11
Rated L-L Voltage (V, rms)	380
Excitation Frequency (Hz)	50

Table 1 Continued

General Information	
Rated Rotating Speed (rpm)	977.876
Number of Poles	6
Motor Length (mm)	280

Simplified stator and rotor shapes are used similar to [68]. Slot shape parameters are listed in Table 2, and other motor parameters for windings and rotor bars are listed in Table 3.

Table 2 Example Induction Motor Slot Shape Parameters

Slot Shapes		
	Stator	**Rotor**
Number of Slots	72	58
Outer Radius (mm)	163.5	104.6
Inner Radius (mm)	105	37.5
Height hs0 (mm)	0.8	0.5
Height hs1 (mm)	40.8	15.5
Width bs0 (mm)	3	1
Width bs1 (mm)	4.8	3.3
Width bs2 (mm)	8.2	3.3

Table 3 Example Induction Motor Parameters

Winding Parameters	
Winding Connection	Star
Number of Parallel Windings	1
Number of Conductors per Slot	6
Coil Pitch	full pitch
Coil D.C. Resistance (Ohm)	0.297292
Coil Lead Inductance (H)	0.000413234
Rotor Bar Parameters	
Electrical Conductivity (S/m)	2.30E+07
End-ring Inter-bar Resistance (Ohm)	7.07241E-07
End-ring Inter-bar Inductance (H)	2.50671E-09

Nonlinear materials are studied. Figure 7 shows the B-H curve for the back iron of material M19_24G_2DSF0.921 that listed in ANSYS Maxwell database.

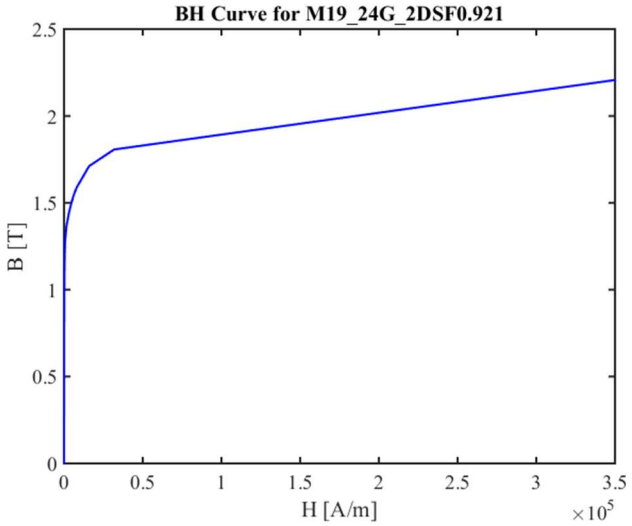

Figure 7 BH curve of magnetic circuit's metal path material

Geometry and Mesh

Figure 8 shows a mesh of the induction motor that generated by the in-house software. A quarter portion of the motor is presented for better visualization of the mesh details. MATLAB PDE Toolbox is used for the mesh generation. As shown, the mesh is adaptively finer in slot area.

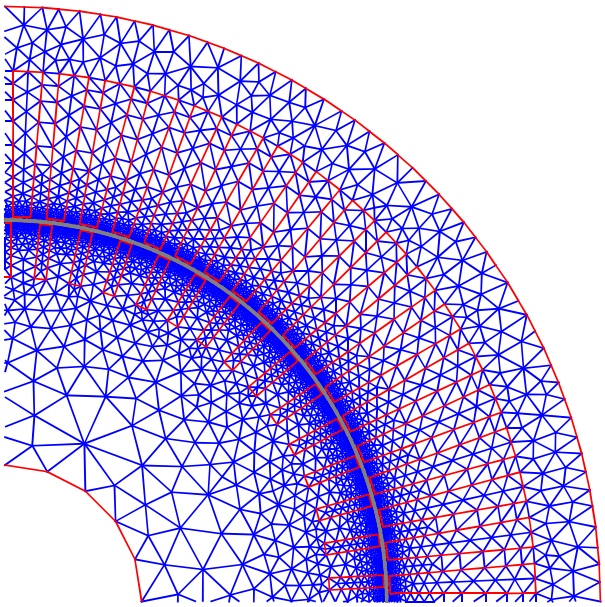

Figure 8 Software Mesh for the Induction Motor

The mesh of the induction motor contains three parts: the static part including the stator, the winding area and slot openings; the rotating part including the rotor, the rotor bar area and rotor side slot openings; and the airgap. The static and rotor mesh were performed separately, and then the "key" nodes on the ring-shape airgap are recorded for airgap region mesh.

The FEM simulation to calculate the eccentric force effects on rotor vibration at rated load condition is discussed below. Simulations of both healthy and faulty machines are studied. The rotor is moved along *x*-axis to simulate the static eccentricity with an eccentricity angle of 0 for simplicity. The simulation is done with a time step of 0.5 micro second of a period of 0 to 0.1 second to reach steady state.

Model Validation

Simulation results of winding current, airgap flux density and the eccentric forces are compared with the ANSYS Maxwell for model validation.

Winding Current

Figure 9 shows the winding current result from the in-house software for the nonlinear motor when at 10% eccentricity. The comparison of the winding current prediction with ANSYS Maxwell shows good agreement.

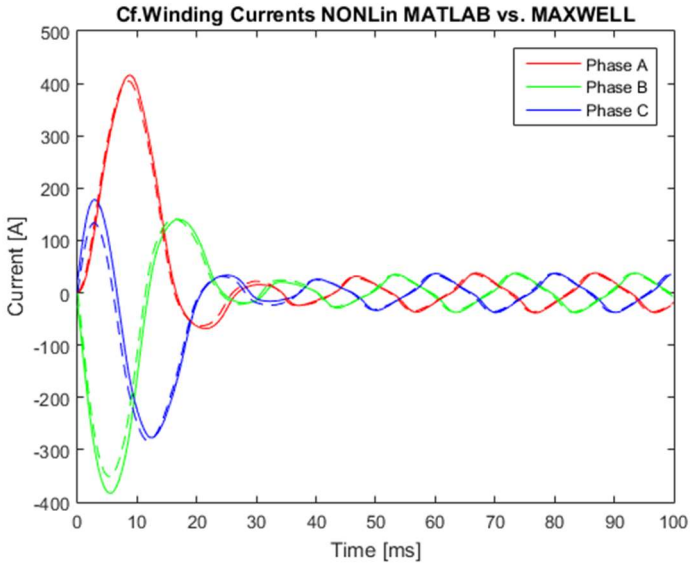

Figure 9 Comparison of Winding Current

Airgap Flux Density

From the figure above, the system starts to get to steady state (i.e. the induced current in rotor bars get to steady state) before t = 50 ms. The comparison of the airgap flux density for the nonlinear induction motor at t = 50 ms are shown as follows. From

the comparison, the predicted air gap radial flux density match well with ANSYS Maxwell results. The tangential flux predicted by the software has higher spikes at slot locations.

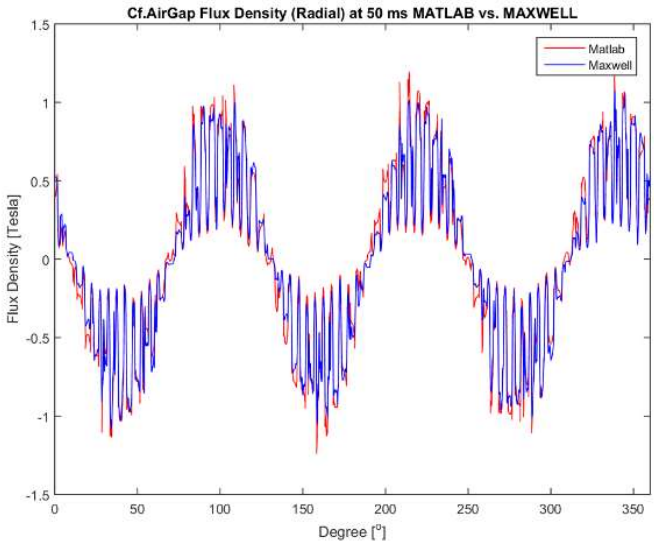

Figure 10 Radial airgap flux density at steady state (50ms)

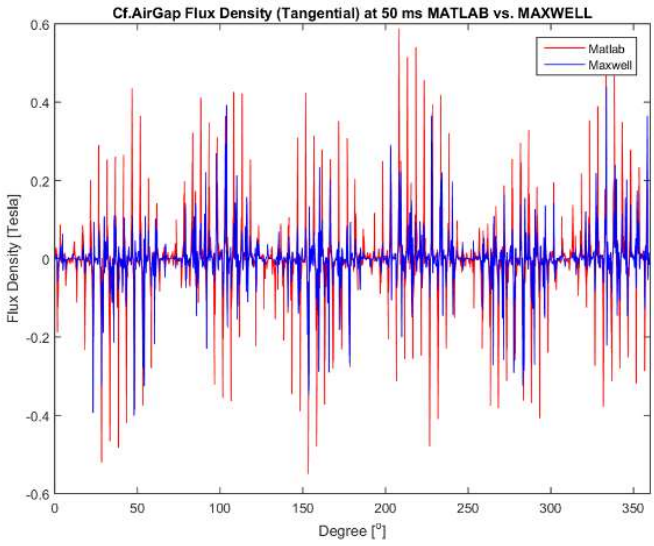

Figure 11 Tangential airgap flux density at steady state (50 ms)

The flux density distribution and equipotential plot (flux lines) of the in-house software and the ANSYS Maxwell results are compared in and Figure 12 and Figure 13 at 50 ms when in steady state.

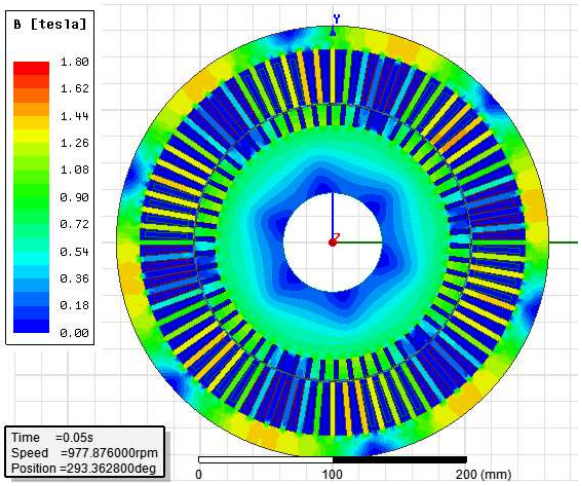

(a) ANSYS Maxwell

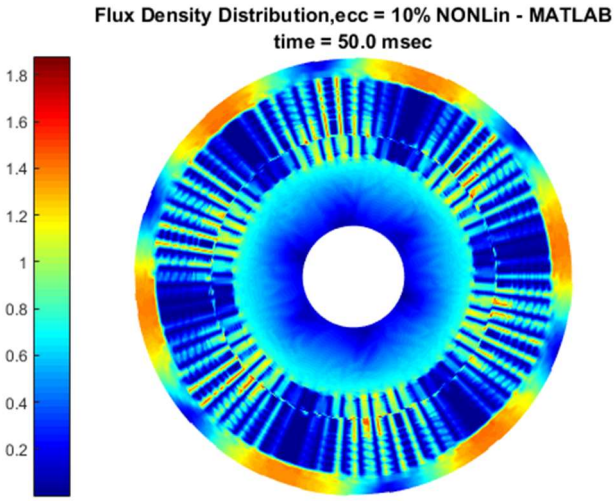

(b) Code

Figure 12 Flux Density Distribution at steady state (t = 50 ms)

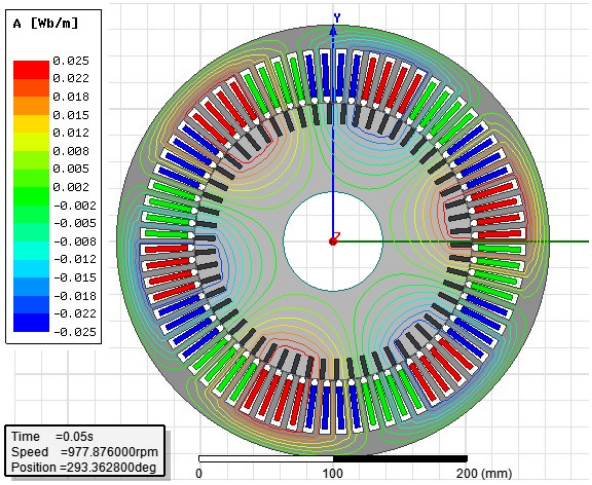

(a) ANSYS Maxwell

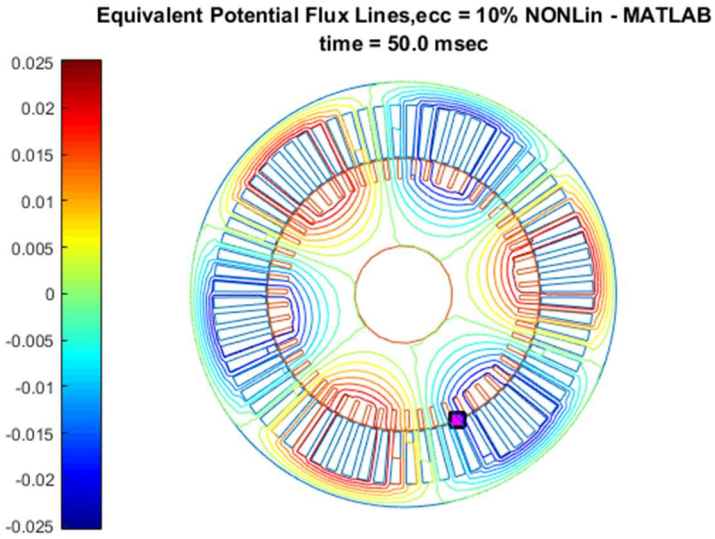

(b) Code

Figure 13 Equipotential (flux lines) plot at steady state (t = 50 ms)

From the comparison above, the field predicted by the in-house software matches very well with ANSYS Maxwell results.

Eccentric Force

When the motor is at 10% eccentricity, comparison of the motor eccentric forces by the in-house software and ANSYS Maxwell are shown as in Figure 14 and Figure 15.

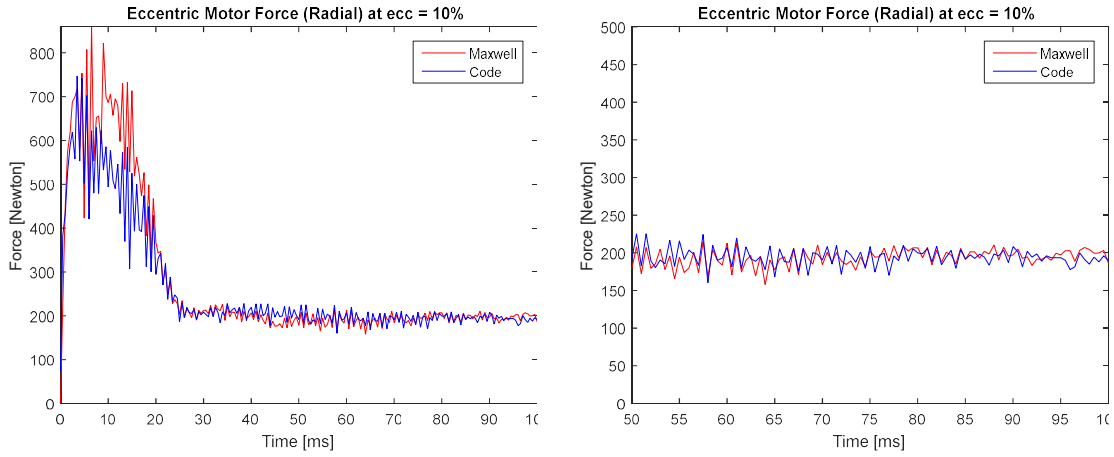

(a) 0-100ms (b) 50-100ms

Figure 14 Motor Eccentricity Force (10%) – Radial

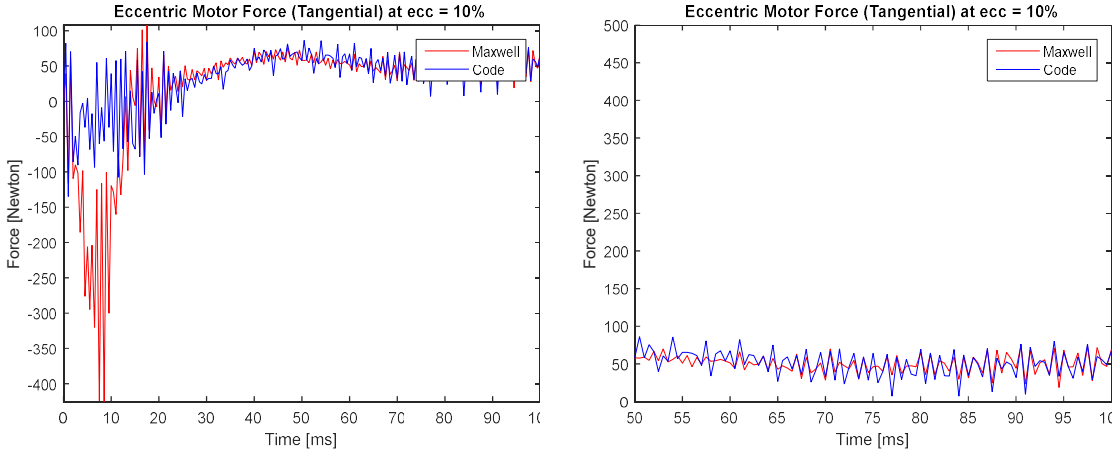

(a) 0-100ms (b) 50-100ms

Figure 15 Motor Eccentricity Force (10%) – Tangential

From the comparison above, the force calculation result of the software is close to the results of ANSYS Maxwell. Both the radial force and tangential force agree with ANSYS Maxwell simulation results, especially when the induction motor runs to steady state.

Difference before steady state might be caused by the different choice of force integration path. In ANSYS Maxwell simulation, the integration is select as a circle. In the in-house software, the path is a set of segments linking the middle points of the triangle's edges. Although theoretically the surface (line as in 2D case) where Maxwell stress tensor force is evaluated can be any as long as inside the airgap, the accuracy can be affected by the choice of integration path in the magnetization process before steady state.

The time period 90-100ms is taken for force calculation, as the system reaches steady state. The radial force is obtained as 191.920 N (2.55% difference from ANSYS Maxwell of 196.943 N) and tangential 51.897 N (0.41% difference from ANSYS Maxwell of 51.686 N).

Parametric Study of Eccentricity Force Effect

The variation of eccentric force as the eccentricity level changes is studied. The motor eccentricity level is changed from 0 mm (0% eccentricity) to 0.28 mm (70% eccentricity) for the example motor, while keeping the same supplied voltage at the rated condition and rotor running at the rated spin speed. Figure 16 shows the eccentric forces

in both directions with cubic curve fitting method. For this example induction motor, the eccentric force can be approximated by the following equation, with FEM results

$$\begin{aligned} F_r &= \quad 3660\times e^3 + 401.9\times e^2 + 3833\times e \\ F_t &= -190.1\times e^3 - 326.1\times e^2 + 998.6\times e \end{aligned} \tag{84}$$

where the eccentricity is in unit millimeter and forces are in unit Newton.

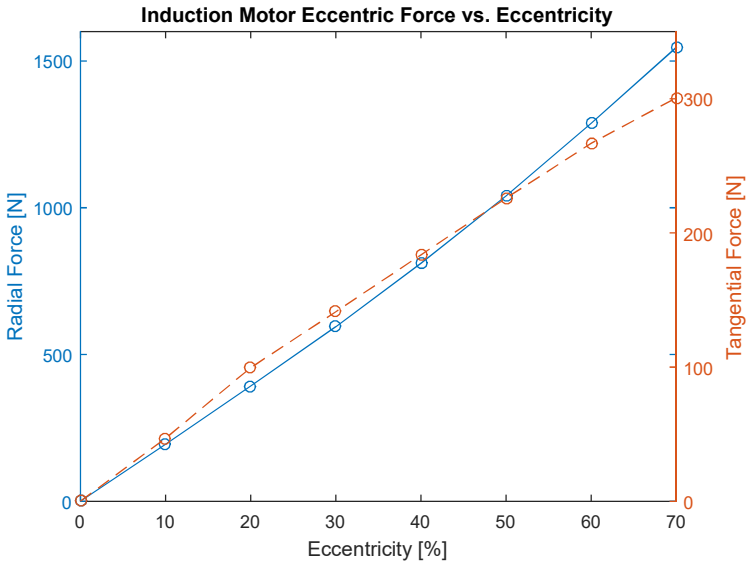

Figure 16 Eccentric Force vs. Eccentricity

The eccentric force results are compared with the results in [24], as an comparison of FEM and MEC.

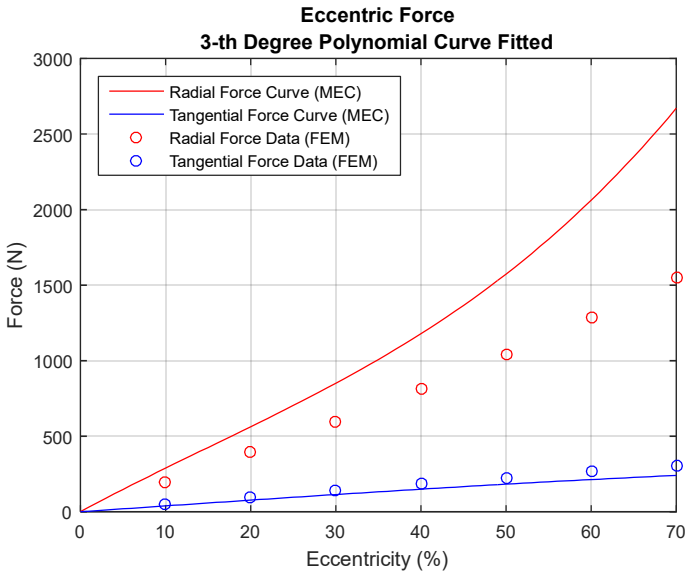

Figure 17 Comparison of Eccentric Force by MEC and FEM

The approximated function in [24] using MEC method is used to generate the curves in Figure 17. Compared with the data points obtained by FEM, MEC predicts a higher eccentricity force in radial direction and smaller in tangential direction. Since MEC utilizes the spatial discretization, results are expected to be less accurate compared to FEM results with less assumption.

Figure 18 shows the cubic-fitted stiffness variation as the eccentricity goes higher.

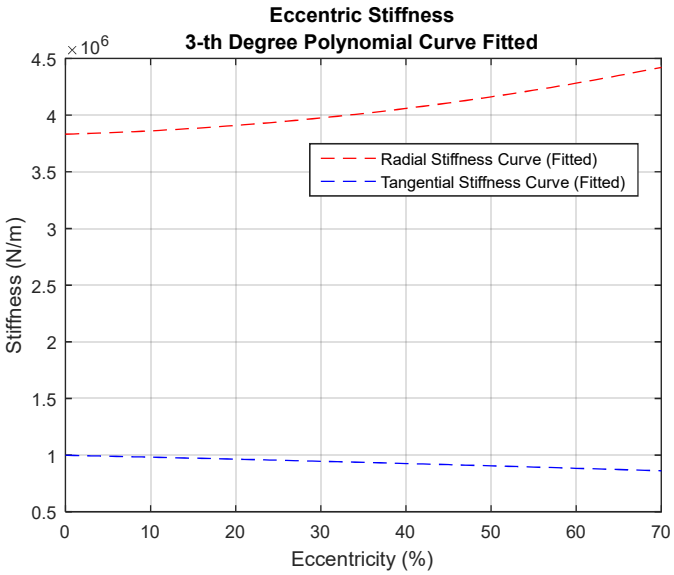

Figure 18 Eccentric Stiffness vs. Eccentricity

The result shows that as radial stiffness increase all the way up as the eccentricity reaches 70%, while tangential stiffness tends to decrease.

Conclusion

Finite element analysis of the induction motor is presented in this chapter. The constant components of the radial and tangential forces are analyzed and compared to commercial software to validate the model. Comparison to literature results is presented as well. Both radial and tangential forces increase nonlinearly with the eccentricity, and can be represented by cubic polynomial function as proposed in [24]. Compared to the results obtained in [24] using MEC, the eccentric forces predicted by FEM have a lower radial component and higher tangential component.

CHAPTER V

ECCENTRIC FORCE CHARACTERISTICS OF PERMANENT MAGNET SYNCHRONOUS MOTOR*

Permanent Magnet Synchronous Motor Formulation

Compared to induction motors, permanent magnet synchronous motor (PMSM) has a unique part of permanent magnets (PM) to model. Common practice is to use equivalent current source method.

Governing Equations for PMSM

The PMs are often characterized by its second-quadrant magnetization, where the PMs often work at. The usual variable for describing a PM is its remnant flux density $\boldsymbol{B}_0$ and its coercive magnetic force H_c (The value is negative since it's in the second quadrant). Relative permeability of PM is usually taken as 1.

If PMs exist in an electric machine, the governing equation of the machine would be updated as

$$\nabla\times(\frac{1}{\mu_0\mu_r}\nabla\times\boldsymbol{A})=\sigma(-\frac{\partial\boldsymbol{A}}{\partial t}-\nabla\boldsymbol{\Phi})-\frac{\partial}{\partial x}\frac{1}{\mu}\boldsymbol{B}_{0y}+\frac{\partial}{\partial y}\frac{1}{\mu}\boldsymbol{B}_{0x} \tag{85}$$

* Part of this section is reprinted with permission from "PM Synchronous Motor Induced Vibration."by Li, Yashu, and Alan Palazzolo. 2018 21st International Conference on Electrical Machines and Systems (ICEMS). IEEE, 2018.

The last two terms are to characterize the PMs, where B_{0x} and B_{0y} are respectively the *x* and *y* components of $\boldsymbol{B}_0$.

The Finite Element Formulation

Apply the Galerkin method to the above equation and circuit equations as derived in previous sections, we will get a system of matrix equations. The only new term shows up that characterizes the PMs is

$$\boldsymbol{M}(i) = \frac{1}{\mu_0 \mu_r} \int_{\Omega_e} \left(\nabla N_i \times \boldsymbol{B}_0 \right) \cdot \boldsymbol{k} \mathrm{d}\Omega \tag{86}$$

Apply the same technique as described in the previous section, the system equations in matrix form describing the PMSM is

$$\begin{aligned} &\boldsymbol{K}\boldsymbol{A} + \boldsymbol{D}\frac{\mathrm{d}}{\mathrm{d}t}\boldsymbol{A} - \boldsymbol{P}\boldsymbol{F}_w\boldsymbol{I}_f^* = \boldsymbol{M} \\ &\boldsymbol{F}_w^{\mathrm{T}}\boldsymbol{Q}\frac{\mathrm{d}}{\mathrm{d}t}\boldsymbol{A} + \boldsymbol{F}_w^{\mathrm{T}}\boldsymbol{R}\boldsymbol{F}_w\boldsymbol{I}_f^* + \boldsymbol{F}_w^{\mathrm{T}}\boldsymbol{L}\boldsymbol{F}_w\frac{\mathrm{d}}{\mathrm{d}t}\boldsymbol{I}_f^* = \boldsymbol{F}_w^{\mathrm{T}}\boldsymbol{F}_w\boldsymbol{U}_f^* \end{aligned} \tag{87}$$

Apply time-discretization method and the system is ready to simulate.

Example Motor Geometry and Parameters

A 6-pole three-phase 20 kW PMSM example with current supply is presented to illustrate the effects of eccentric operation on transverse motor forces and rotor vibrations. The magnetic fields and forces are determined. The motor has 36 stator slots, and its cross section is shown in Figure 19.

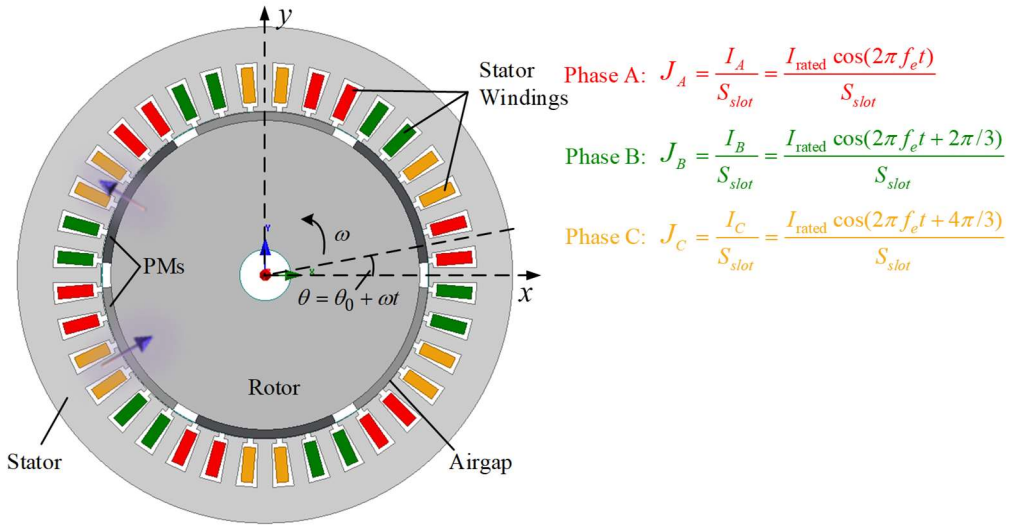

Figure 19 Cross section of the motor showing the rotor, stator, magnets, windings and air gap.

Similarly, the FEM model of the motor in Figure 19 is full, since the eccentricity introduces an asymmetry that precludes usage of a symmetry model. A zero value for the magnetic potential is specified on the outer boundary as a means of setting the normal magnetic flux density to zero on the boundary. Phase balanced sinusoidal currents excite the stator windings to produce a rotating magnetomotive force (MMF). The permanent magnets in each rotor pole are modeled as neodymium-iron-boron (NdFeB) type and are magnetized radially (as shown by the purple arrows in the figure). The main parameters and material properties for this motor are listed in Table 4 and Table 5.

Table 4 Motor Related Parameters

Main Parameter	Unit	Value
Rated power P_{rated}	kW	20
Rated current (RMS) I_{rated}	A	92
Supply frequency f_e	Hz	50
Rotating speed ω	rpm	1000
Stator outer diameter D_{os}	mm	340
Stator inner diameter D_{is}	mm	225
Rotor outer diameter D_{or}	mm	224
Rotor inner diameter D_{ir}	mm	35
No. of permanent magnets	--	6
Permanent magnet thickness h	mm	6
Permanent magnet embrace α	--	0.85
Coil pitch z	--	2
Winding Layer(s)	--	1
No. of slots	--	36
Motor length l	mm	100
Motor air gap g_0	mm	0.5

Table 5 Motor Material Properties

	Material	Properties	
Winding	Copper	**Relative permeability** μ_r	1
Back iron	Silicon Steel M19	**Nonlinear BH curve**	
Permanent Magnet	NdFeB XG196/96	**Residue flux density** B_r	0.91 T
		Coercive force H_c	-726.962 kA/m
		Relative permeability μ_{rPM}	1

Figure 20 shows the nonlinear BH curve for the magnetic circuit's metal path.

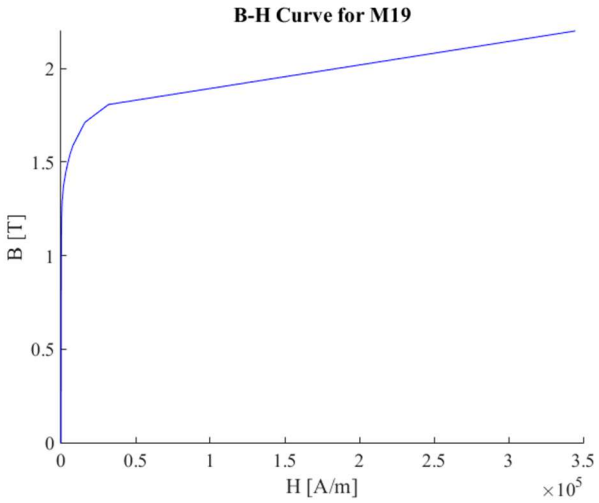

Figure 20 BH curve of magnetic circuit's metal path material M19

The FEM simulation to calculate the eccentric force effects on rotor vibration at rated load condition is discussed below. Simulations of both healthy and faulty machines are studied. The rotor is moved along *x*-axis to simulate the static eccentricity with an eccentricity angle of 0 for simplicity.

The mesh is shown in Figure 21 and has a finer grid in the air gap region to obtain increased accuracy of the predicted field.

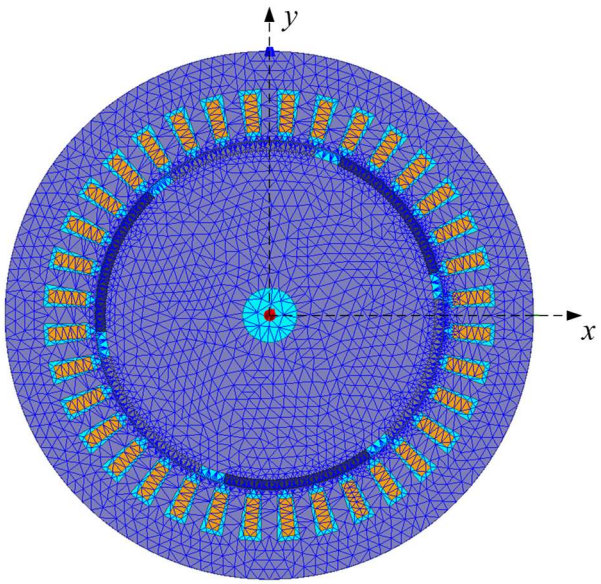

Figure 21 Finite element mesh for the PMSM magnetic potential

Model Validation

Airgap flux density

Airgap flux density at steady state is compared to validate the model. The system runs to steady state at 150 ms and chosen to be the time spot for airgap flux density comparison. Airgap flux density when the motor is at 10% eccentricity is shown below in Figure 22 and Figure 23.

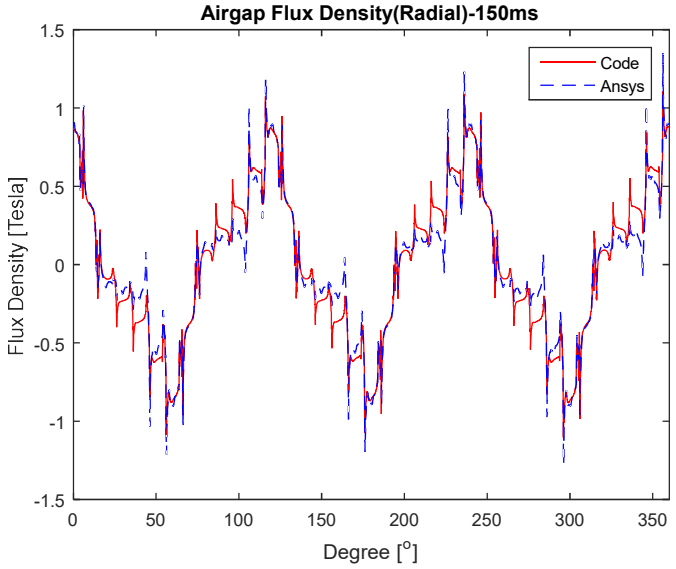

Figure 22 Comparison of airgap flux density at steady state – Radial

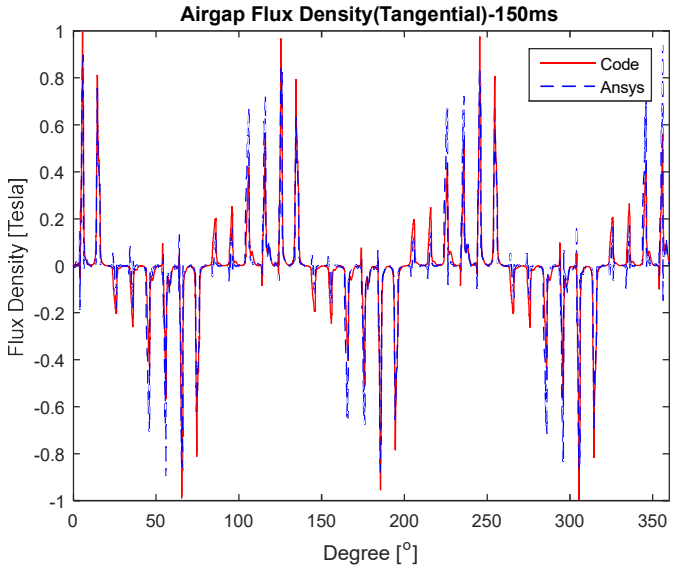

Figure 23 Comparison of airgap flux density at steady state – Tangential

The airgap flux density from the code simulation matches well with the result from the ANSYS Maxwell simulation. Frequency analysis is performed to analyze the

frequency components. Figure 24 and Figure 25 show the frequency spectrum of the airgap flux density in radial and tangential direction respectively.

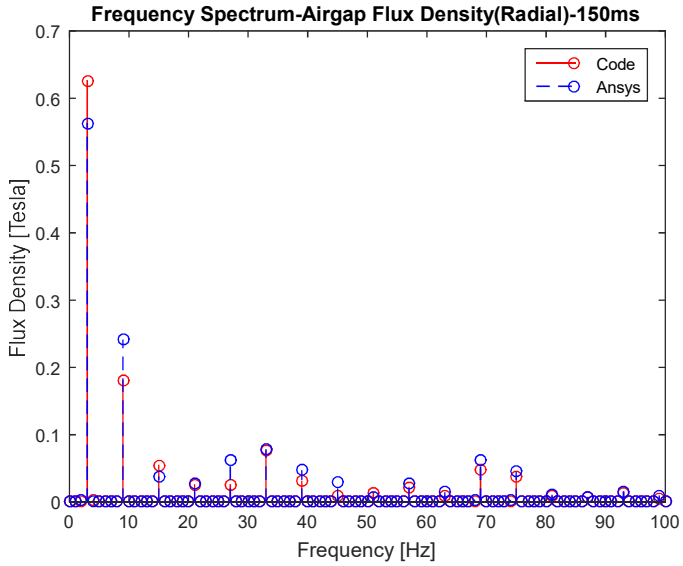

Figure 24 Comparison of airgap flux density spectra at steady state – Radial

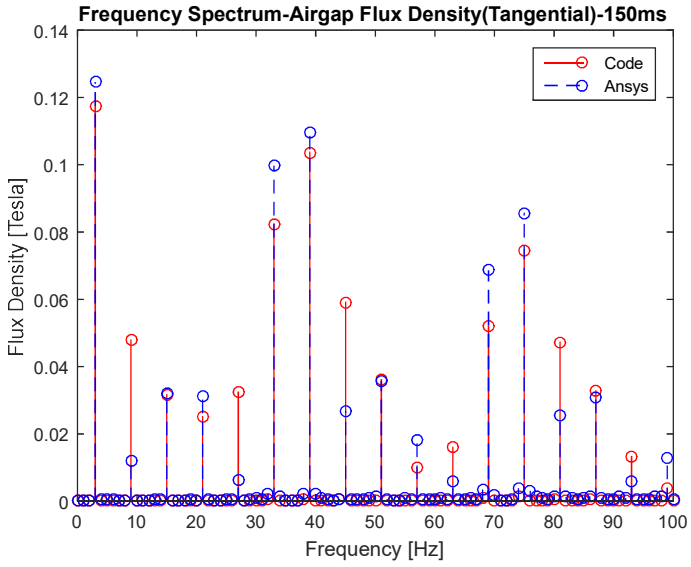

Figure 25 Comparison of airgap flux density spectra at steady state – Tangential

From the above analysis, the airgap flux density agrees well both in time domain and frequency domain.

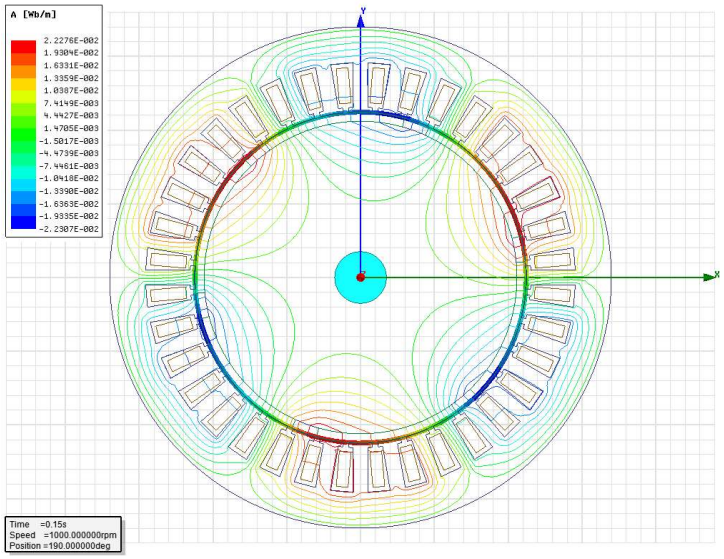

(a) ANSYS Maxwell

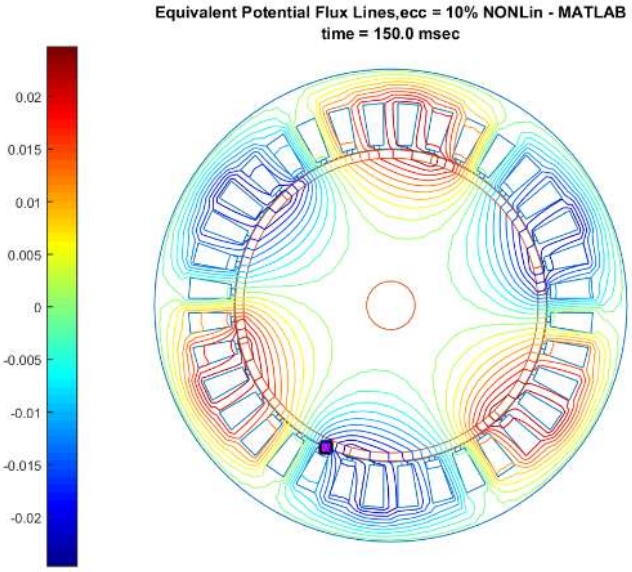

(b) Code

Figure 26 Equipotential (flux lines) plot at t = 150 ms

The flux density distribution and equipotential plot of solver and the ANSYS Maxwell model are compared in Figure 26 and Figure 27 at 150 ms when in steady state.

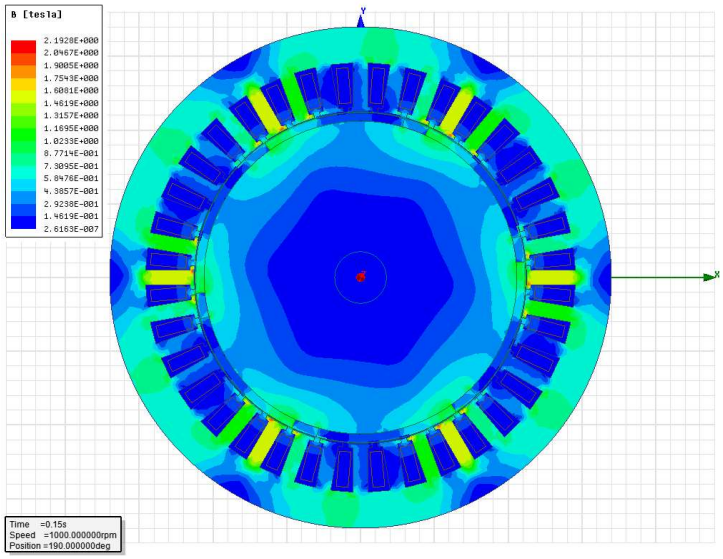

(a) ANSYS Maxwell

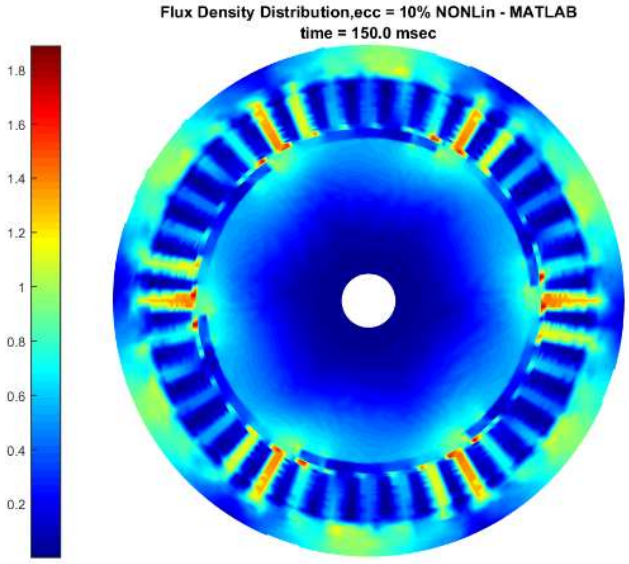

(b) Code

Figure 27 Flux Density Distribution at t = 150 ms

From the comparison above, both the flux lines plot and the field distribution predicted by the code matches very well with ANSYS Maxwell results. At steady state, the predicted field is close for the two simulations.

Eccentric Force

When the motor is at 10% eccentricity, comparison of the motor eccentric forces by the code and ANSYS Maxwell are shown as in Figure 28.

As shown, before steady state, the code and ANSYS results differ from each other; however, the forces are approximately the same when runs to steady state. For this example PMSM, when at 10% eccentricity, the constant component of the radial eccentric force is around 40 N for both code and ANSYS results.

Figure 29 shows that radial force spectra agree well: constant component (known as the eccentric force, UMP), 50Hz, 100 Hz and 600 Hz. Detailed frequency analysis of the force will be presented in the following section.

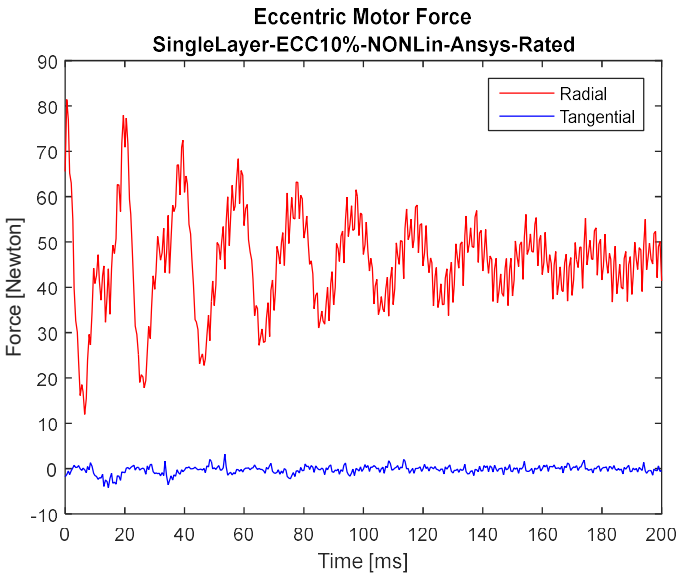

(a) ANSYS Maxwell

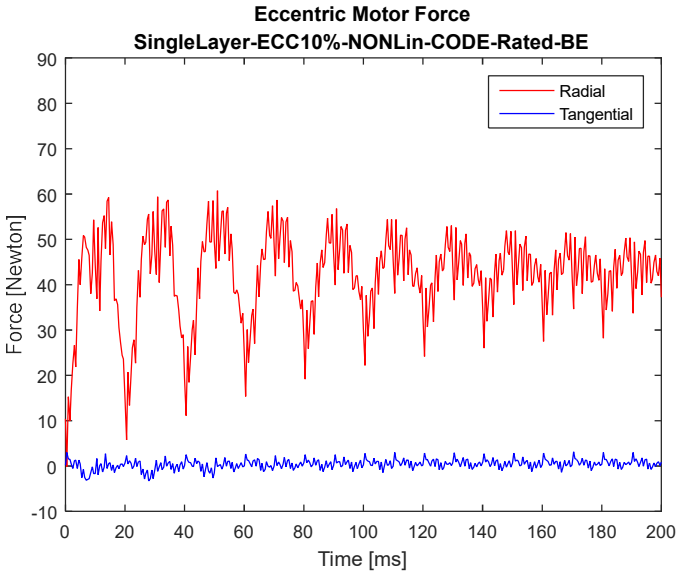

(b) Code

Figure 28 Motor Eccentric Force Comparison

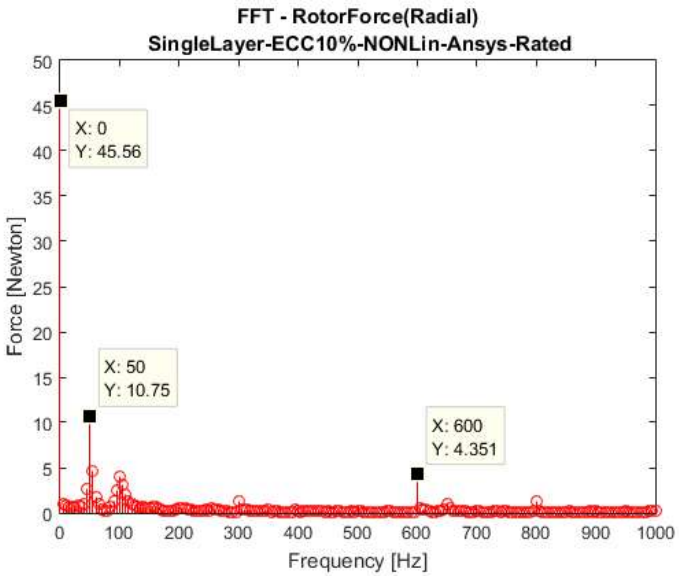

(a) ANSYS Maxwell

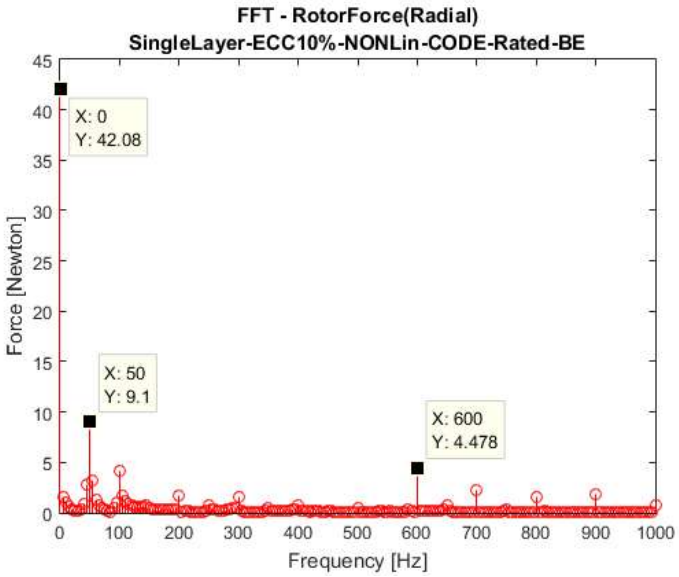

(b) Code

Figure 29 Motor Eccentric Force Spectra Comparison – Radial

Radial and Tangential Airgap Flux Density and Eccentric Force

The eccentricity causes a variation of the airgap around the circumference between the rotor and stator. Figure 30 shows the radial and tangential airgap flux density at steady state when there is no eccentricity and when the rotor is 50% eccentric. For both radial and tangential directions, the symmetry of the flux density no longer holds if the motor is eccentric. The flux density will get higher at locations where the airgap is narrower (0-90 and 270-360 degrees) and the flux density is lower at other locations.

Figure 31 shows the radial and tangential flux densities at a given point in the middle of the narrowest airgap, vs. time for an eccentricity of 50% when the system reaches steady state.

The corresponding frequency spectra are shown in Figure 32. Both radial and tangential flux densities contain frequency components of odd multiples of the supply frequency $\left(50\times(2N+1)\text{ Hz},\ N=1,2,3...\right)$.

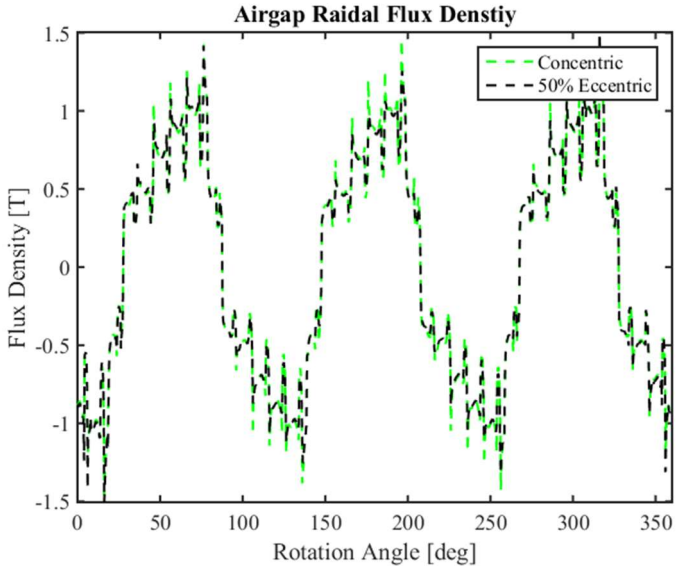

(a) Radial flux density

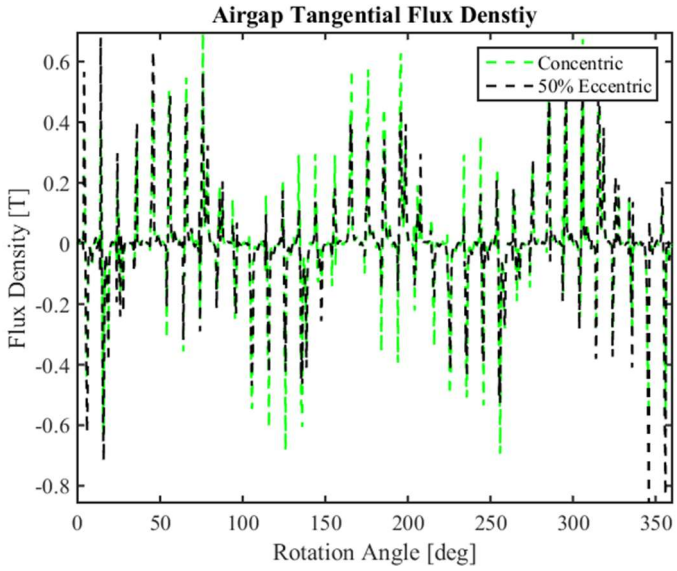

(b) Tangential flux density

Figure 30 Comparison of airgap flux density without eccentricity and with eccentricity 50% at steady state (t=142 ms)

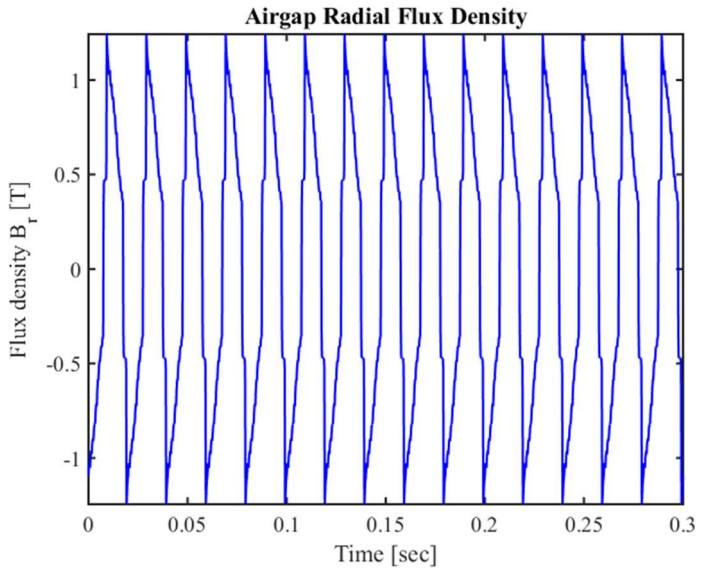

(a) Radial flux density

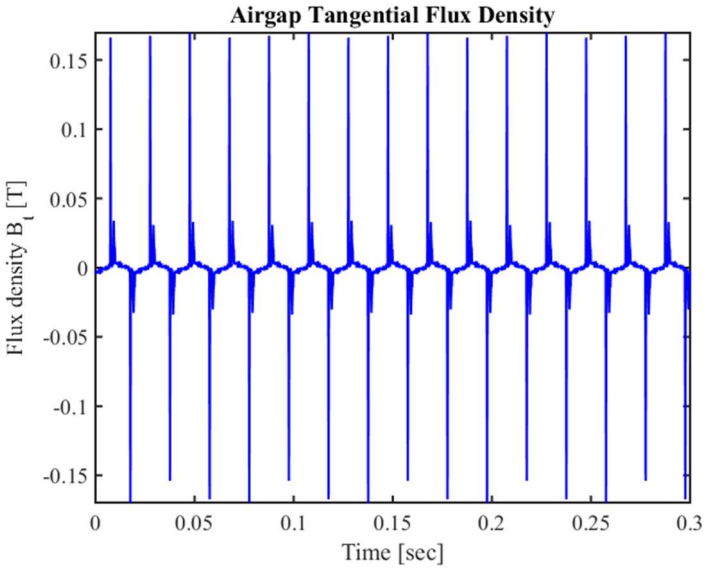

(b) Tangential flux density

Figure 31 Time history of airgap flux densities at a point with eccentricity 50%.

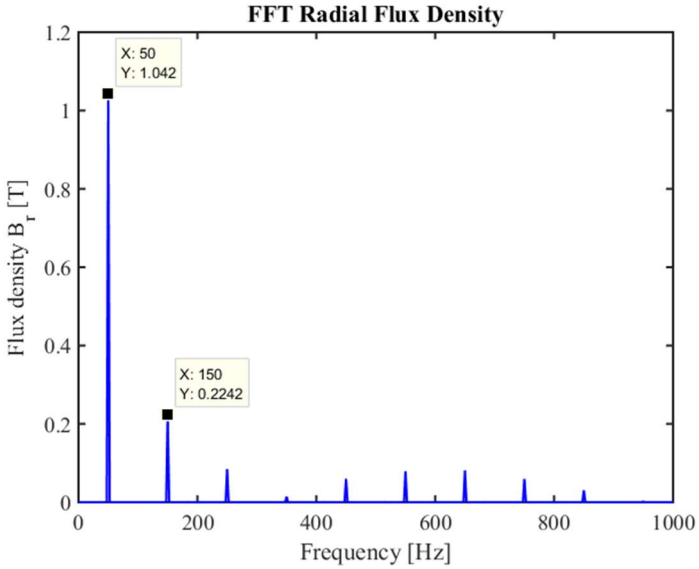

(a) Radial flux density

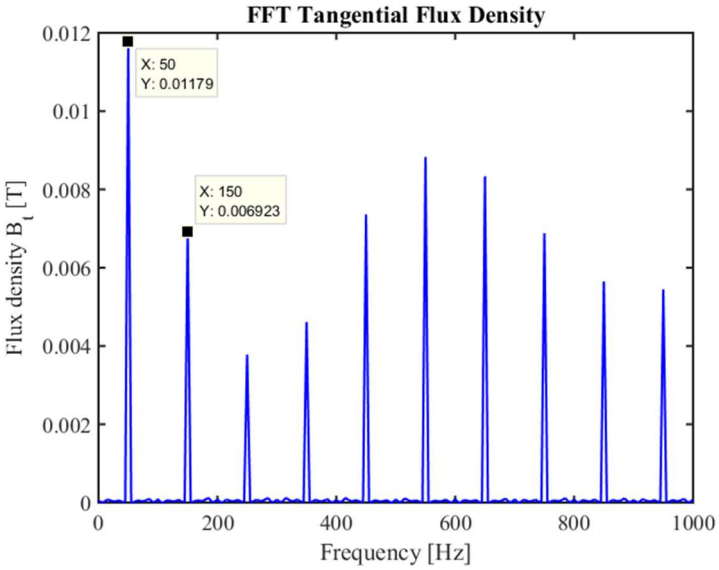

(b) Tangential flux density

Figure 32 Spectra of airgap flux densities at a point with eccentricity 50%.

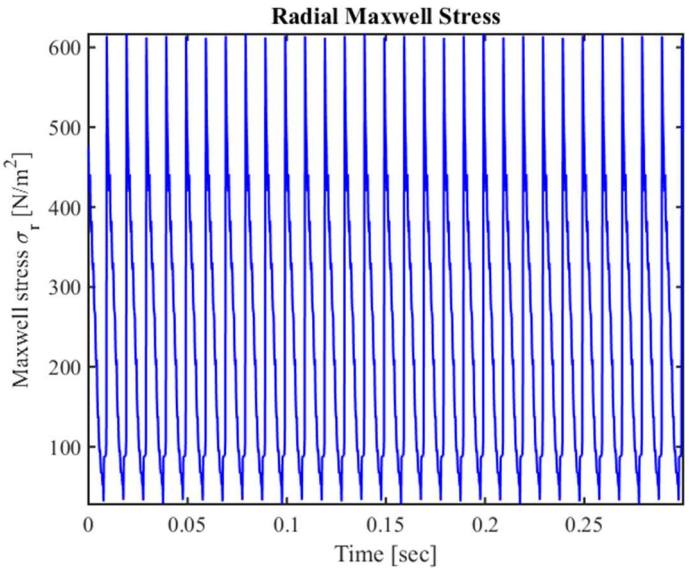

(a) Radial Maxwell stress

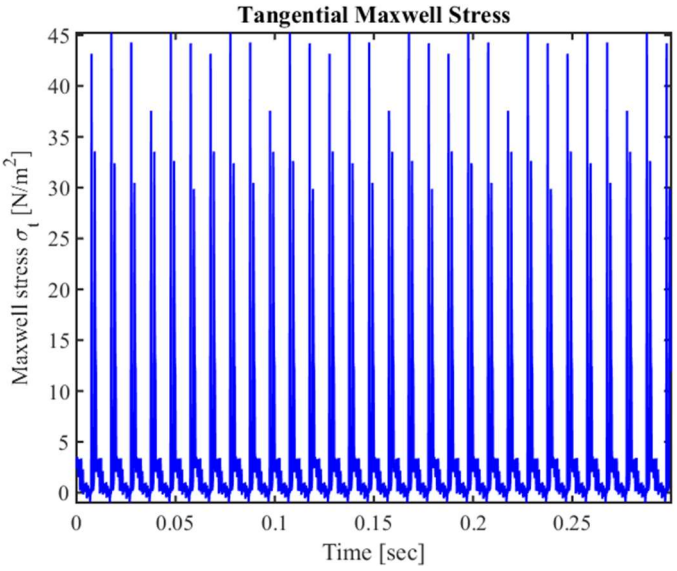

(b) Tangential Maxwell stress

Figure 33 Time history of Maxwell stresses of a point with 50% eccentricity.

Figure 31 and Figure 33 show that the fundamental period of both the radial and tangential Maxwell stress is half of that of the radial and tangential flux density. Thus,

the Maxwell stresses have frequency components at even multiples of the supply frequency components, as shown in Figure 34.

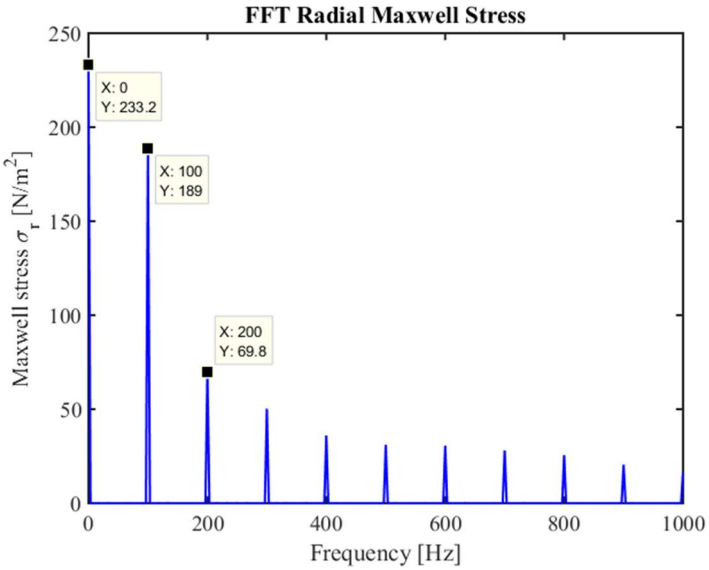

(a) Radial Maxwell stress

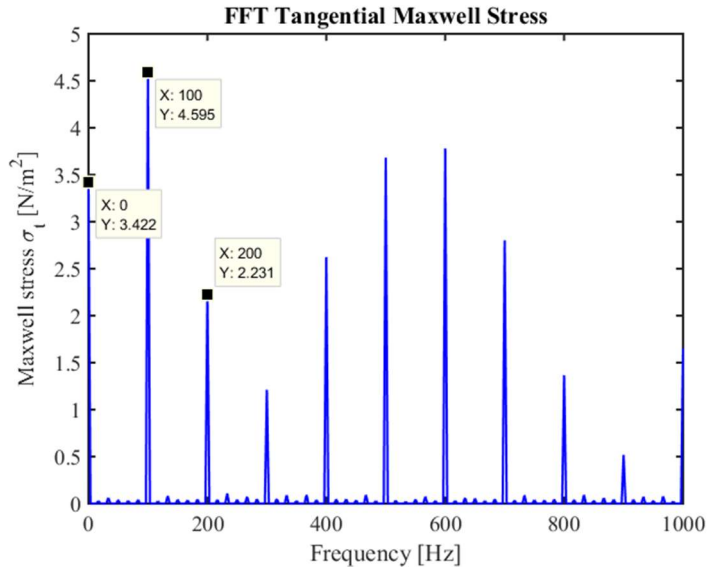

(b) Tangential Maxwell stress

Figure 34 Spectra of Maxwell stresses at a point with 50% eccentricity.

These frequencies relationships can be understood from trigonometry, where squaring a sin or cosine results in doubling of the frequency. This is explained in approximate analytical methods for eccentricity force, where tangential components are usually omitted. The explanation follows with:

(1) The fundament MMF can be expressed as a sinusoidal function of the input power frequency.

(2) This gives the radial and tangential flux densities also a frequency component of the input power frequency.

(3) The square of the flux densities in the Maxwell stresses yields a doubling of the frequency of that of flux density, i.e. double the input power frequency.

Parametric Study of Eccentricity Force Effect

The degree of rotor/stator eccentricity, the input current level and the air gap are varied to illustrate the sensitivity of the transverse forces to changes in these variables.

Eccentricity

The radial and tangential eccentric forces are shown in Figure 35 for different levels of eccentricity.

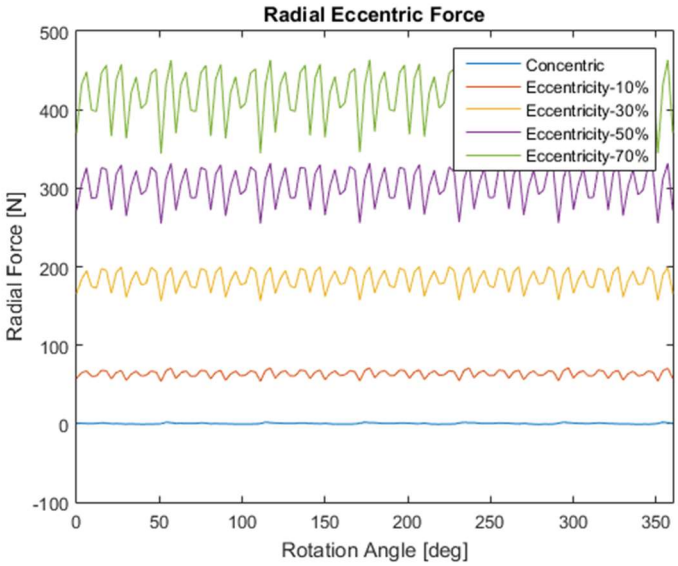

(a) Radial eccentric force

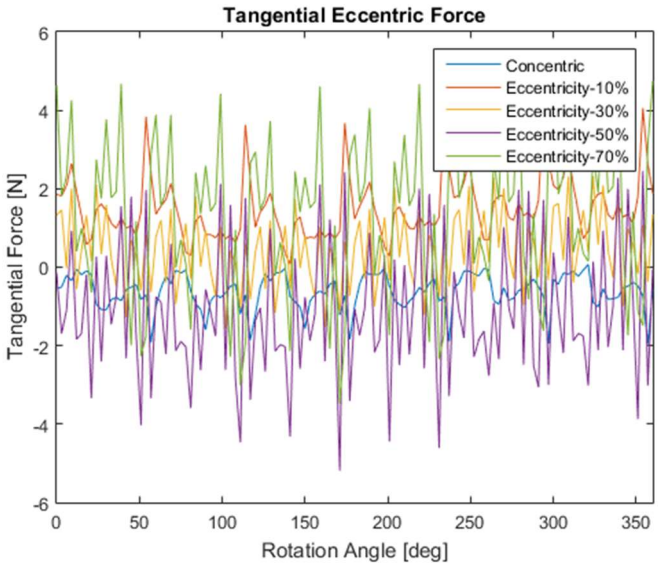

(b) Tangential eccentric force

Figure 35 Eccentric force with selected different eccentricity level.

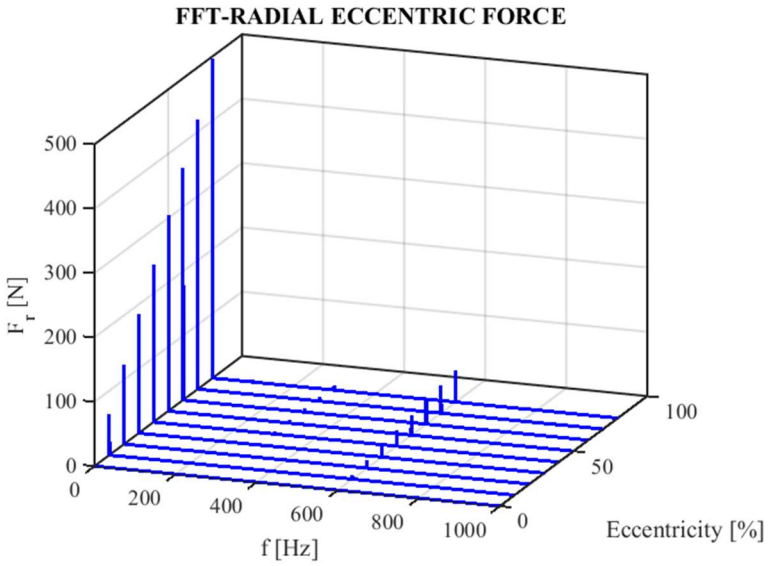

(a)

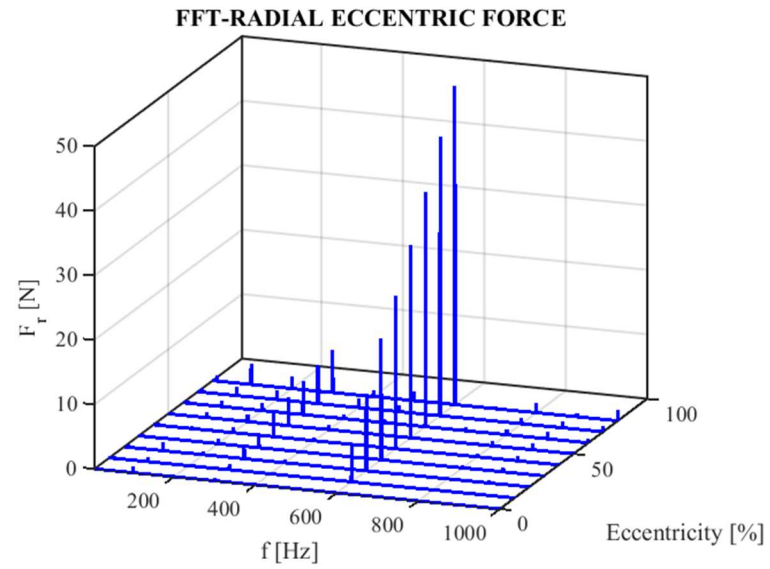

(b)

Figure 36 Spectra of the radial eccentric force. (a) Including constant component; (b) Excluding constant component

Figure 35 shows that the radial and tangential harmonics of forces increase with increasing eccentricity, however the tangential force component is much smaller than the radial. The amplitudes of the harmonics are much smaller than the constant (order zero) component, but all are increasing with eccentricity. This is shown in Figure 36. The highest amplitude harmonic is around 8% of the constant component and occurs at

$$600\ \text{Hz} = \frac{rotating\ speed\,(1000\ \text{rpm})}{60\ \text{sec/min}} * (no.\ of\ \ stator\ slots = 36)\ \text{Hz} \qquad (88)$$

Other harmonics occur at the rotor spinning frequency (16.67 Hz) and even multiples of the supply frequency $\left(50 \times (2N)\ \text{Hz},\ \ N = 1, 2, 3...\right)$. The radial force constant component is plotted vs. rotor/stator eccentricity in Figure 37.

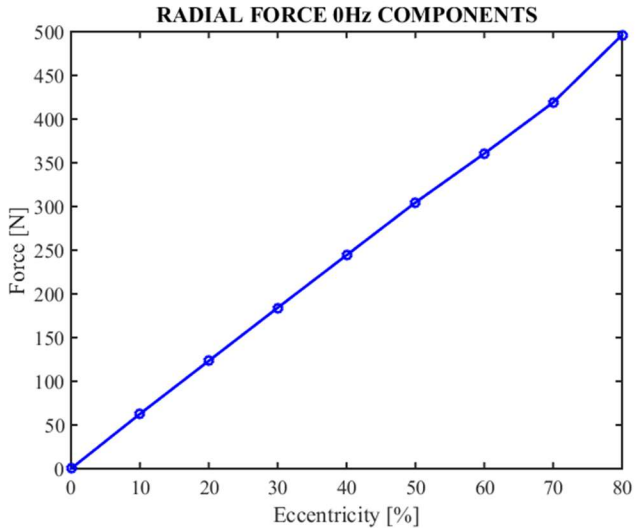

Figure 37 Constant component of the radial motor force vs. motor/stator eccentricity.

The time average (constant component) radial force is an approximate linear function of eccentricity as illustrated in Figure 37, so

$$F_{r\text{con}} = k_{\text{negative}} e \tag{89}$$

where $F_{r\text{con}}$ is the constant force component in Newton; e is the eccentricity in meters; and k_{negative} is the negative stiffness caused by the magnetic force, and determined to be 1.224×10^{6}N/m for the example PMSM simulated under rated conditions. Negative indicates the eccentric force direction is always pointing towards the direction of the eccentricity.

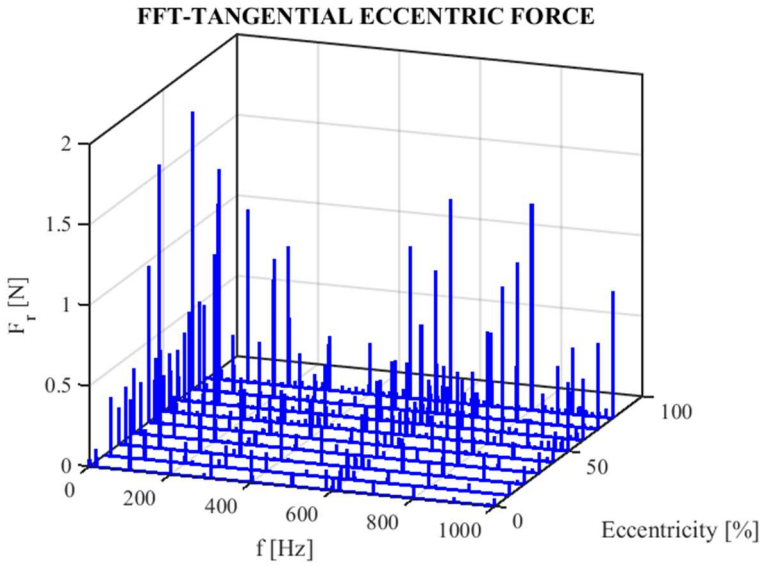

Figure 38 Spectra of the tangential eccentric force vs. eccentricity.

Figure 38 shows the spectra of the tangential eccentric force. The average tangential force is very small relative to the average radial force, and the spectra contains harmonics at rotor spinning frequency as well as even multiples of supply frequencies.

From the above analysis, the radial and tangential eccentric forces can be written as:

$$F_r = F_{r\text{con}} + F_{r\text{har}}$$
$$F_t = F_{t\text{har}} \tag{90}$$

where $F_{r\text{con}} = k_{\text{negative}} \cdot e$ as defined in Equation (89) represents the constant part of the radial eccentric force. $F_{r\text{har}}$ denotes the harmonics of the radial eccentric force.

The constant part of tangential force F_t is negligible thus the tangential eccentric force contains primarily the harmonics part.

Input Current

The motor radial forces vary as the motor operating current changes. The input phase RMS current is changed from 55.2A to 368 A while the motor eccentricity and spin speed are kept at 0.35mm (70%) and 1000 rpm, respectively. The motor rated current is 92A. It is assumed the insulation of the motor would allow for the simulated high input currents.

Figure 39 shows radial and tangential transverse forces for selected input currents. The constant component of radial eccentric force tends to decrease as the input current increases, while the harmonics seem nearly invariant with current level for both radial and tangential transverse forces. Note that the dominant frequency is 600 Hz which is 6 times twice the line frequency, indicating that the number of magnets (6) has a strong effect on the time varying forces. The field from the permanent magnets dominates the electromagnetic field, which explains why the forces appear nearly invariant with drive current.

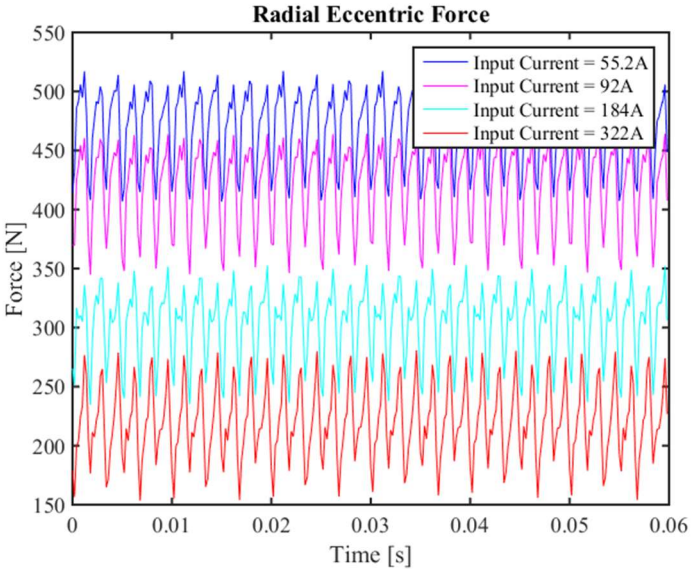

(a) Radial eccentric force

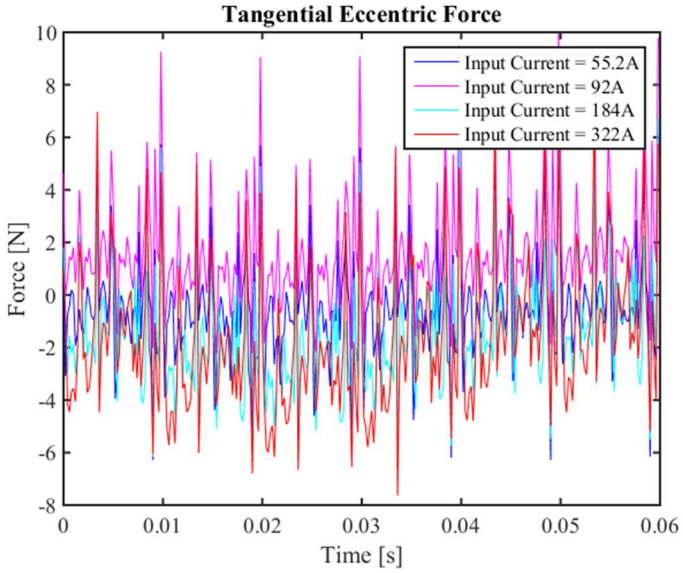

(b) Tangential eccentric force

Figure 39 Eccentric forces with different input currents (RMS) at 70% static eccentricity.

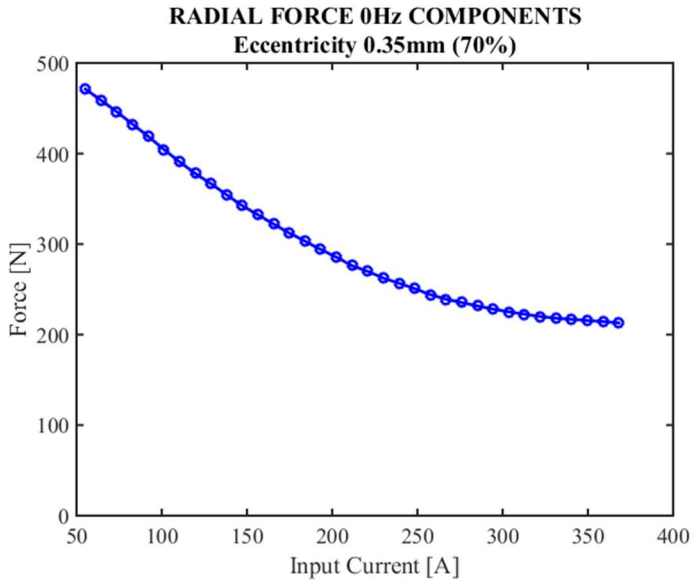

Figure 40 The constant component of the transverse radial force vs. input current (RMS) at 70% static eccentricity.

Figure 40 shows the constant component of the transverse radial force vs. input current. The radial force decreases and approaches saturation as the current increases. This is due to the dominance of the permanent magnet field. As the input current increases, the field produced by the windings increase, which mitigates the unbalanced field caused by the motor rotor eccentricity.

Figure 41 shows that the force magnitude at 16.67Hz in both radial and tangential directions are almost identical with radial force slightly higher. Both the radial and tangential forces at the spin frequency increase as the input current increases. They continue to increase before and after reaching the rated current and then approach saturation.

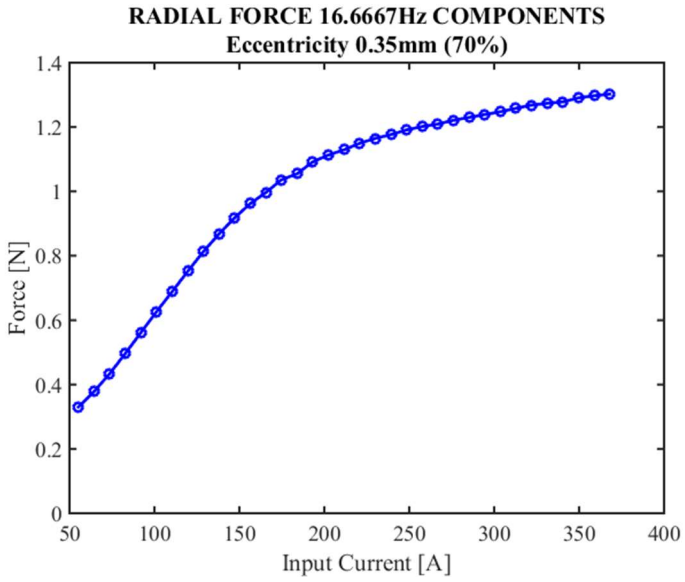

(a) Radial eccentric force

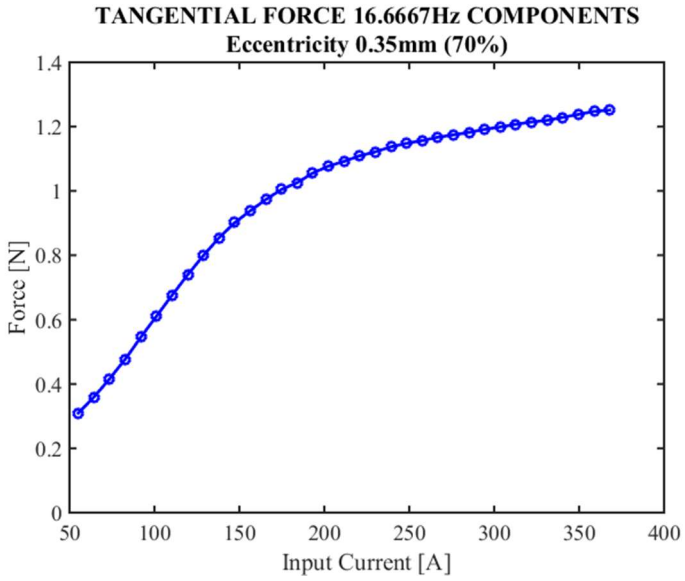

(b) Tangential eccentric force

Figure 41 Eccentric force magnitude at 16.67Hz vs. input current (RMS).

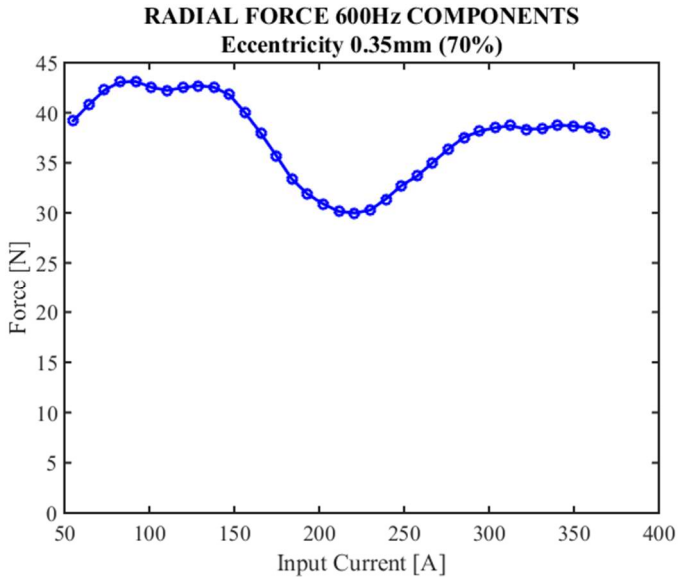

(a) Radial eccentric force

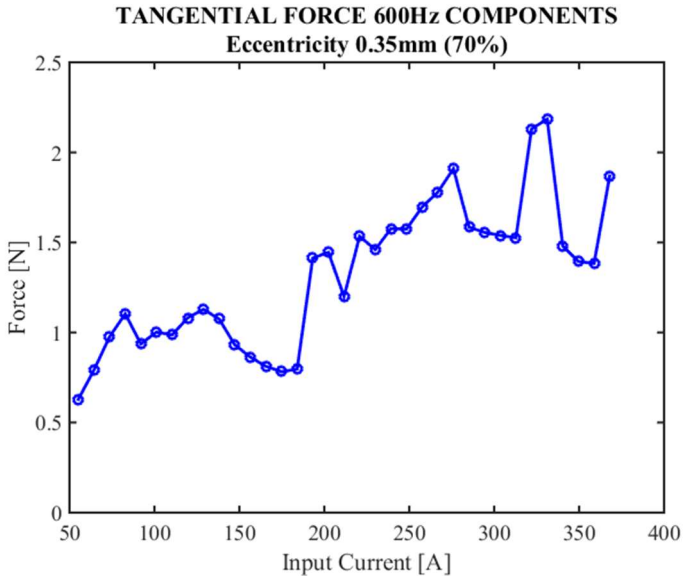

(b) Tangential eccentric force

Figure 42 Eccentric force magnitude at 600Hz with different input currents at 70% static eccentricity.

Magnitudes of other frequency components of the transverse forces appear to vary about average values as the input current changes. Figure 42 shows the magnitudes of the 600Hz component.

Air-gap Variation

The above results correspond with a 0.50 mm nominal air gap between the centered rotor and stator. The following results demonstrate how the motor's transverse forces change with variation of the air gap about its nominal value. The air gap is changed by raising or lowering the inner diameter of the stator, while keeping the remainder of the rotor and stator geometrical and material parameters constant. The supply current is maintained at its nominal value (92A RMS), as is the spin speed (1000 rpm). The eccentric distance remains constant at (0.1mm) for all cases studied.

Figure 43 shows the radial and tangential transverse forces for the nominal and three additional air gaps where the eccentric distance was kept the same.

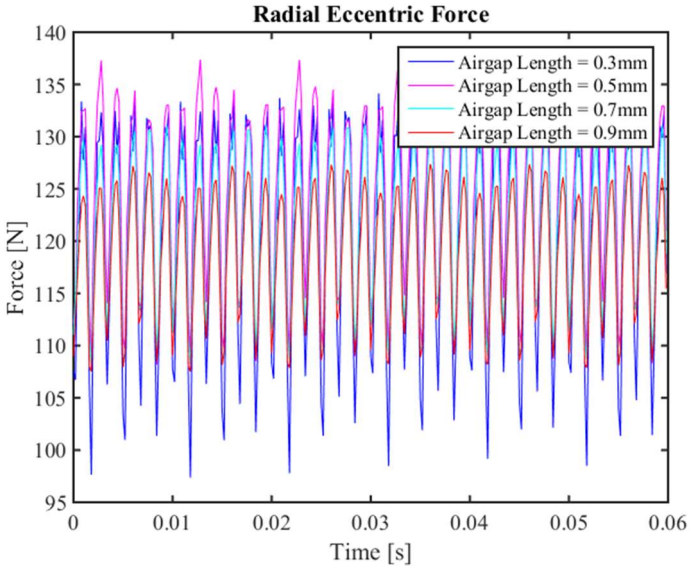

(a) Radial eccentric force

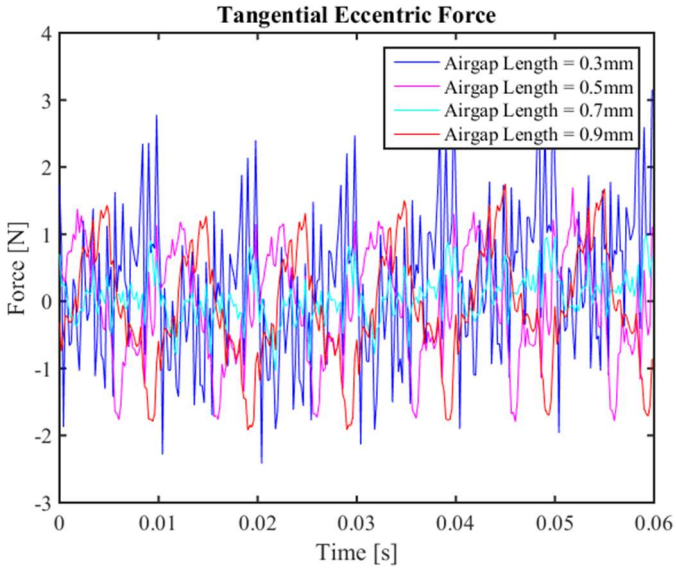

(b) Tangential eccentric force

Figure 43 Transverse forces with a 0.1mm eccentric distance and various air gaps.

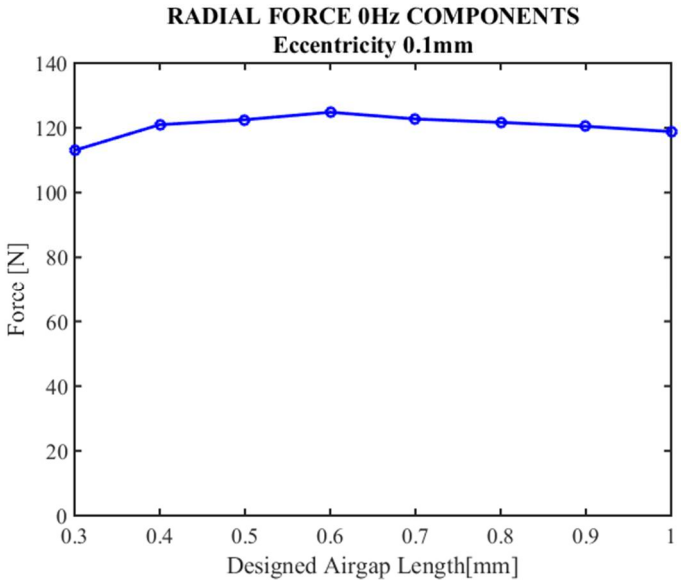

Figure 44 The constant (zero order) component of the radial force vs. airgap length with an eccentric distance of 0.1mm.

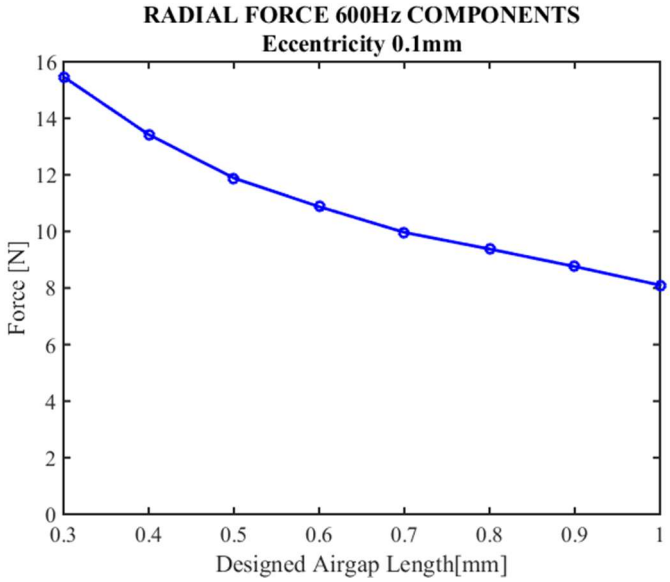

(a) Radial tangential force

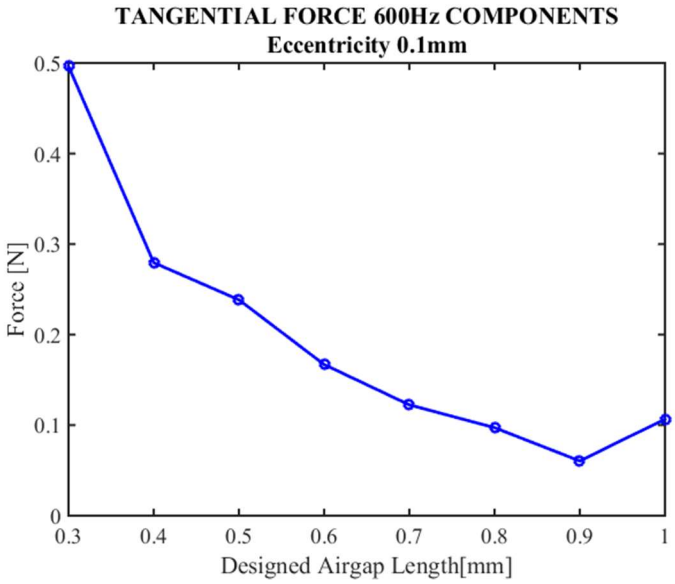

(b) Tangential eccentric force

Figure 45 The transverse force's 600 Hz component vs. air gap length.

Figure 44 shows that the constant (zero order) component of the radial force is nearly invariant with changes in the air gap. This occurs even though the air gap changes cause the relative eccentricity to vary from a low of 10% with the airgap at 1mm, to a high of 33% with the air gap at 0.3 mm. The reason for this behavior is that the permanent magnet's thickness of 6 mm is much larger than the air gap, so that the permanent magnet provides a strongly dominant reluctance.

Figure 45 shows that the 600Hz component of the radial and tangential transverse forces decrease with increasing air gap length. The magnitudes of the remaining frequency components tend to be invariant with air gap length.

Conclusion

Finite element analysis of the example PMSM is presented in this Chapter. The radial component of the motor induced transverse force consists of a constant component and harmonics. The frequency of the harmonics occurs at the rotor spin frequency and even multiples of the supply frequency. The dominant harmonic of radial eccentric force occurs at a frequency related to the number of stator coil slots and the number of magnets. The tangential force contains harmonics at the same frequencies as the radial force.

CHAPTER VI

ECCENTRIC FORCE EFFECTS ON DYNAMICS[†]

Effects of Motor Static Eccentricity on Rotor Vibration

Consider the anomalous case when the bearing centerline has a parallel offset relative to the centerline of the motor stator, causing the motor to operate with a static eccentricity. Further assume that the bearings are relatively stiff relative to the motor's magnetic pull so that rotor deflections relative to the bearing centerline are much smaller than the motor air gap. Thus, the resulting rotor's position with respect to the stator centerline consists approximately of a constant static eccentricity distance, plus a small deviation with respect to the bearing centerline.

Figure 46 shows the example's rotor model including a massless shaft supporting a lumped mass and in turn supported by two bearings, each with a stiffness of $k/2$ and a damping of $c/2$. The rotor is placed on the *x*-axis with a constant offset from the stator center (*z*-axis in the figure) to simulate the static eccentricity. The rotor rotates about its own axis with an angular speed of ω and has a mass unbalance distance of e_m as shown.

[†] Part of this section is reprinted with permission from "PM Synchronous Motor Induced Vibration." by Li, Yashu, and Alan Palazzolo. 2018 21st International Conference on Electrical Machines and Systems (ICEMS). IEEE, 2018.

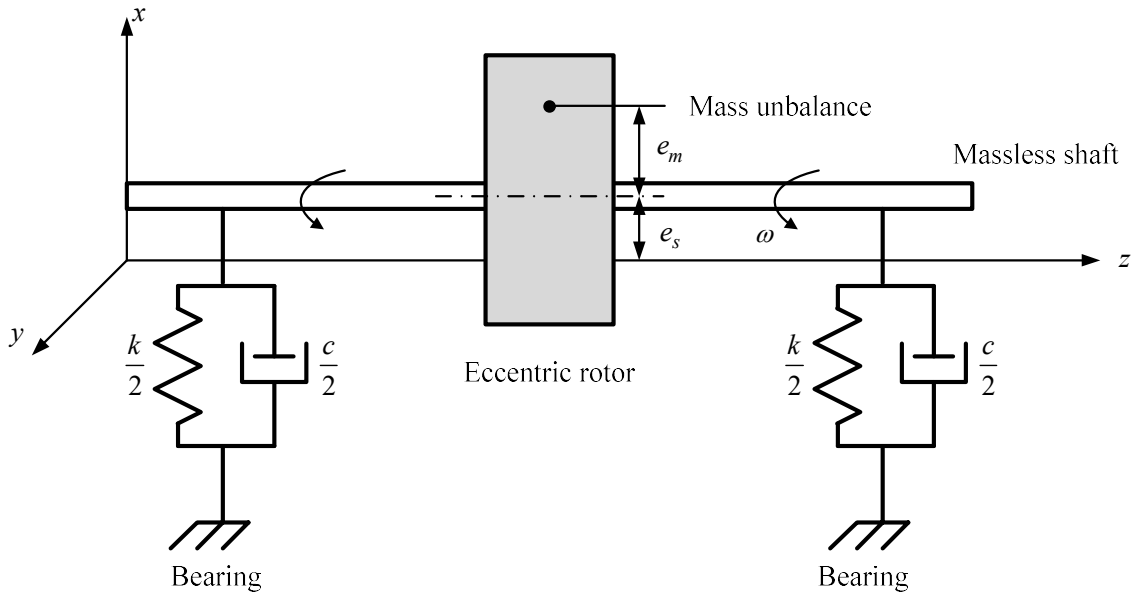

Figure 46 Rotordynamics model of the mass unbalanced rotor offset from the stator centerline and supported by stiff bearings.

The PMSM's rotor has an initial static eccentricity e_s and precesses (vibrates) about this position due to the combined effects of the motor eccentricity forces and the rotor's mass imbalance forces, as illustrated in Figure 47.

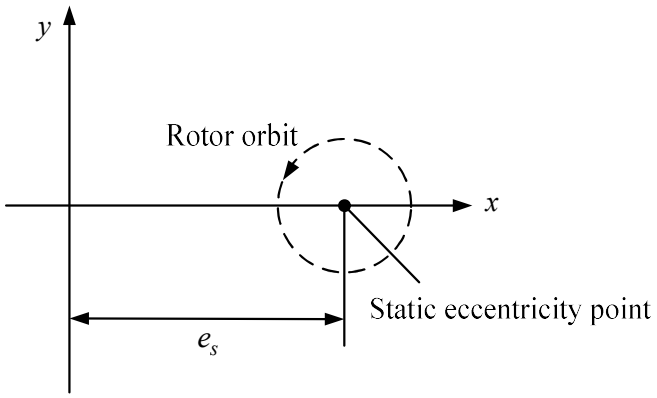

Figure 47 Rotor precessing about static eccentricity location.

Equations of Motion

A Jeffcott rotor model is utilized to study the effect of motor eccentricity induced forces on shaft vibration. The Jeffcott rotor represents the shaft and the combined motor rotor and attached disk masses lumped together as mass m and concentrated in the middle of the rotor (shaft). The combined bearing lateral motion stiffness is k and damping is c . The equations of motion are

$$\begin{aligned} m\ddot{x} + c\dot{x} + k(x - e_s) &= me_m\omega^2 \cos(\omega t) + F_x \\ m\ddot{y} + c\dot{y} + ky &= me_m\omega^2 \sin(\omega t) + F_y \end{aligned} \tag{91}$$

where e_m is the mass unbalance; ω is the rotor spin speed; t is time; x and y are rotor lateral motions in corresponding directions; e_s is the initial static eccentricity due to misalignment; F_x and F_y are motor eccentric forces in the x and y directions and are obtained from the following equation, with eccentricity angle θ shown in Figure 1.

$$\begin{Bmatrix} F_x \\ F_y \end{Bmatrix} = \begin{bmatrix} \cos\theta & -\sin\theta \\ \sin\theta & \cos\theta \end{bmatrix} \begin{Bmatrix} F_r \\ F_t \end{Bmatrix} \tag{92}$$

where the transverse forces $F_r = k_{\text{negative}}x + F_{r\text{har}}$ and $F_t = F_{t\text{har}}$, result from Equation (89) and (90). The force harmonics terms and are obtained from the magnetic field/force FEM simulations and are interpolated vs. motor angle in the numerical integration of Equation (91). The approach is valid with the assumption that the rotor system vibrates near the static eccentricity point utilized in the FEM field simulation.

The equation of motion can be written in matric form as

$$\boldsymbol{M}\begin{Bmatrix}\ddot{x}\\ \ddot{y}\end{Bmatrix}+\boldsymbol{C}\begin{Bmatrix}\dot{x}\\ \dot{y}\end{Bmatrix}+\boldsymbol{K}\begin{Bmatrix}x\\ y\end{Bmatrix}=\begin{Bmatrix}me_m\omega^2\cos(\omega t)\\ me_m\omega^2\sin(\omega t)\end{Bmatrix}+\boldsymbol{F} \tag{93}$$

where $\boldsymbol{M}=\begin{bmatrix}m & 0\\ 0 & m\end{bmatrix}$, $\boldsymbol{C}=\begin{bmatrix}c & 0\\ 0 & c\end{bmatrix}$, $\boldsymbol{K}=\begin{bmatrix}k_{\text{eq}} & 0\\ 0 & k_{\text{eq}}\end{bmatrix}=\begin{bmatrix}k-k_{\text{negative}} & 0\\ 0 & k-k_{\text{negative}}\end{bmatrix}$,

$\boldsymbol{F}=\begin{Bmatrix}ke_s\\ 0\end{Bmatrix}+\begin{Bmatrix}F_{x\text{har}}\\ F_{y\text{har}}\end{Bmatrix}$, $\begin{Bmatrix}F_{x\text{har}}\\ F_{y\text{har}}\end{Bmatrix}=\begin{bmatrix}\cos\theta & -\sin\theta\\ \sin\theta & \cos\theta\end{bmatrix}\begin{Bmatrix}F_{r\text{har}}\\ F_{t\text{har}}\end{Bmatrix}$.

Write the equations of motion in first order form, with $\boldsymbol{X}=\begin{Bmatrix}x\\ y\end{Bmatrix}$ and $\boldsymbol{V}=\begin{Bmatrix}\dot{x}\\ \dot{y}\end{Bmatrix}$,

$$\begin{Bmatrix}\dot{\boldsymbol{X}}\\ \dot{\boldsymbol{V}}\end{Bmatrix}=\begin{bmatrix}\boldsymbol{0} & \boldsymbol{I}\\ -\boldsymbol{M}^{-1}\boldsymbol{K} & -\boldsymbol{M}^{-1}\boldsymbol{C}\end{bmatrix}\begin{Bmatrix}\boldsymbol{X}\\ \boldsymbol{V}\end{Bmatrix} \tag{94}$$

The numerically integrated solutions run until steady state is reached, with the initial conditions $\begin{bmatrix}e_s & 0 & 0 & 0\end{bmatrix}^T$ since the coordinate system center is set as the stator center.

Time Domain Simulation and Numerical Analysis

The Jeffcott Rotor model parameters are

$$m=13.9\text{ kg},\ k=1.9833\times10^8\text{ N/m},\ c=104.6\text{ N.s/m} \tag{95}$$

and mass unbalance $e_m=0.01\text{mm}$, and initial condition of $e_s=0.35\text{mm}$ (70%).

The rotor system damped natural frequency without the motor's negative stiffness is

$$f_d=\frac{\sqrt{k/m-(c/2m)^2}}{2\pi}=601.86\text{Hz} \tag{96}$$

Results of the numerical integration solution for the Jeffcott rotor response are provided below for cases with and without motor static eccentricity and using 2 magnetic force models: the motor's transverse force average only and the motor's full transverse force. The mass unbalance effects are included for all cases.

Centered Rotor-Zero Eccentricity Case

The sole excitation source for this case is mass unbalance. Displacements and orbits are shown in Figure 48.

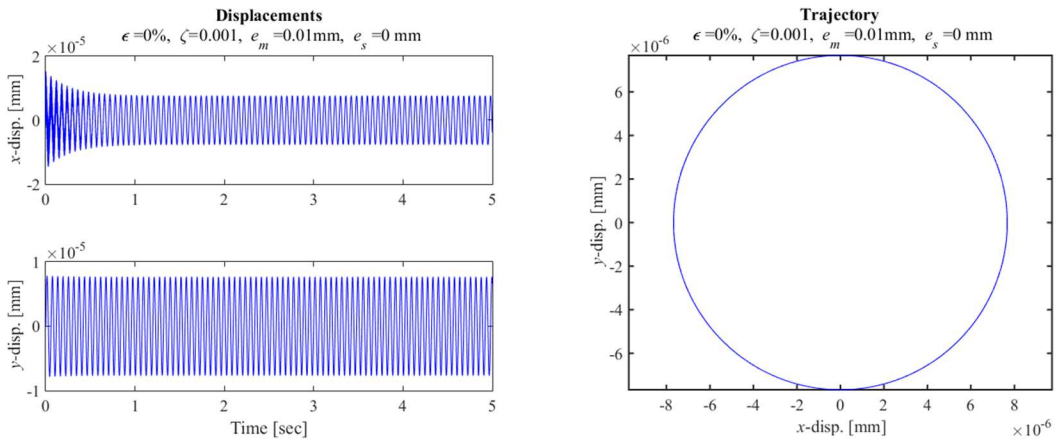

(a) (b)

Figure 48 Rotor system response without motor eccentricity forces applied. (a) displacements; (b) orbit.

The spectra of the x and y direction displacements are shown as below in Figure 49. Different frequency ranges (0-10Hz, 10-50Hz, 50-550Hz and 550-1000Hz) are plotted separately to better view all frequency components in the range of interest. The system displacements have dominant frequency components at the spin frequency (16.67 Hz) due to the imbalance forces. Vibration near the natural frequency (600Hz) is at a

very low level. The maximum vibration amplitude at steady state is very small of 7.7×10-6 mm.

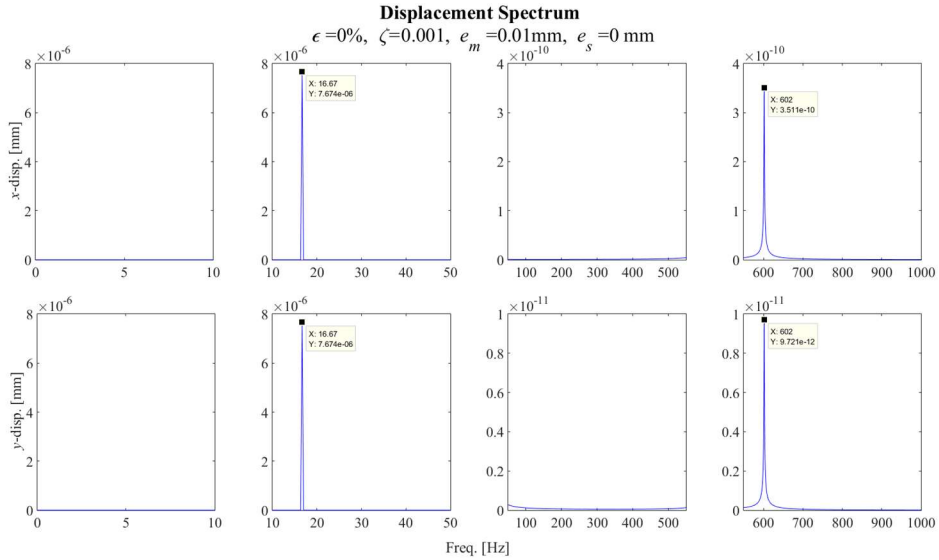

Figure 49 Displacement spectra of the rotor system without motor/stator eccentricity effects.

Eccentric System with Constant Eccentric Force

Harmonics of the eccentric system forces are omitted in this case. Only the constant (average) of the radial transverse force, as represented with the negative stiffness, and imbalance are applied. The displacements and orbit of the system are shown in Figure 50.

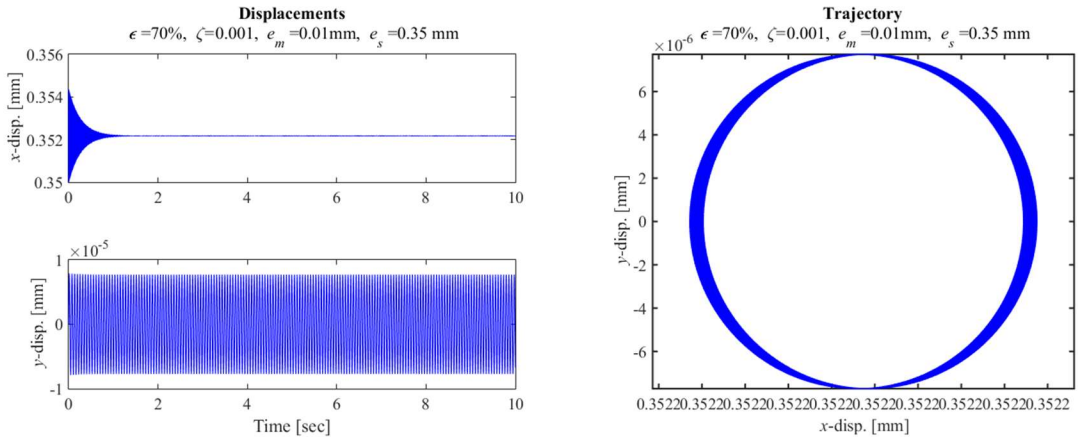

(a) (b)

Figure 50 Rotor system response with only the constant radial transverse force applied. (a) displacements; (b) orbit.

The rotor has an initial static eccentricity of 0.3500 mm due to misalignment, however the orbit center moves slightly to 0.352 mm due to the motor's negative stiffness (magnetic pull). The orbit is ring-like with variations of "thickness" of the ring along the x-axis. This results from the motor eccentricity induced force having a component near to the natural frequency (601Hz). The resulting vibration is comparable to the dominant vibration at 16.67 Hz at 7.78×10^{-6} mm, as illustrated in the displacement spectra in Figure 36. The vibration in this case is at a very low level.

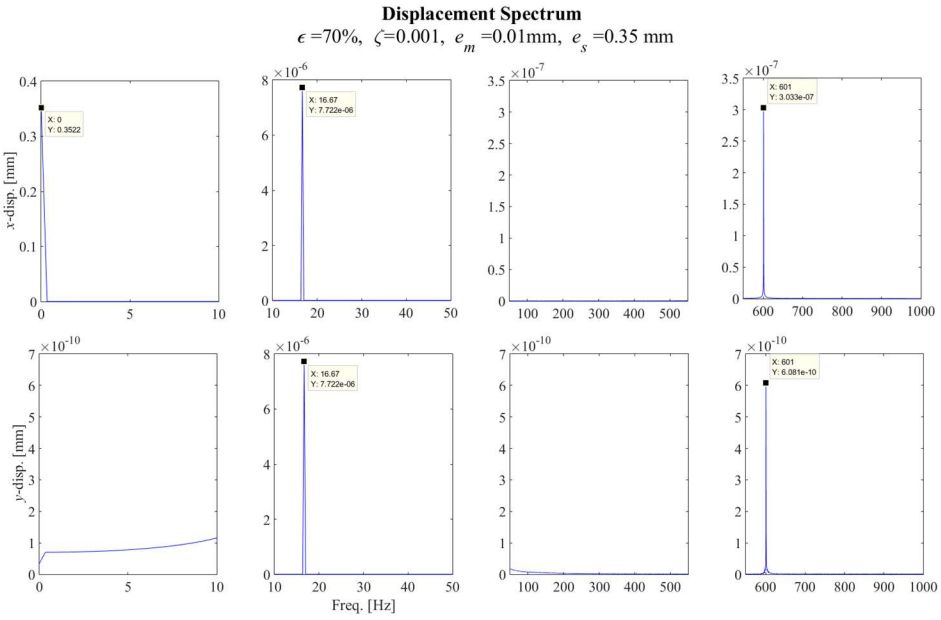

Figure 51 Displacement spectra of the rotor system under the effect of the constant (average) radial transverse motor force

Rotor System with Full Motor Eccentric Forces Applied

The full time history of the motor's eccentric forces are applied to the rotor in this case. The radial and tangential force harmonics at a motor static eccentricity of 0.35mm (70%) are shown as below in Figure 52.

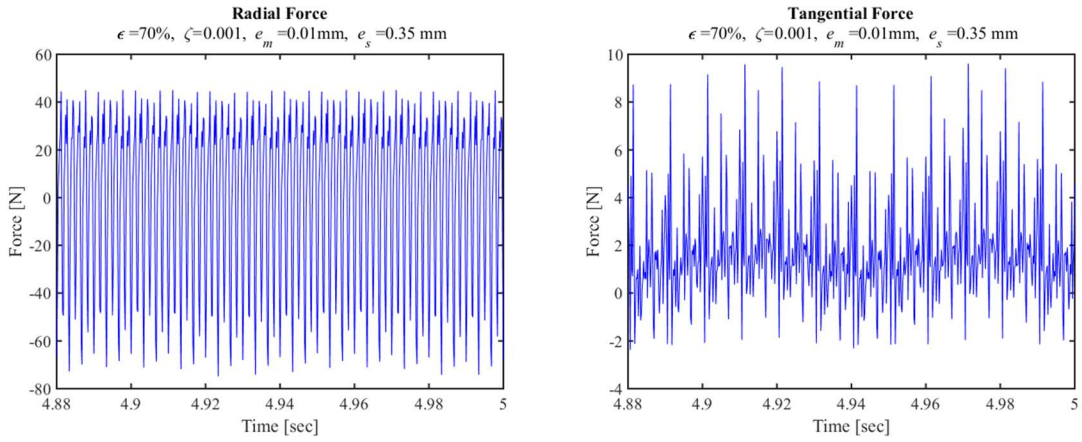

(a) (b)

Figure 52 Harmonics of the eccentric motor forces applied to the rotor system (constant component not included). (a) radial force; (b) tangential force.

Figure 53(a) shows the x and y displacements, and Figure 53(b) shows the steady state orbit of the rotor.

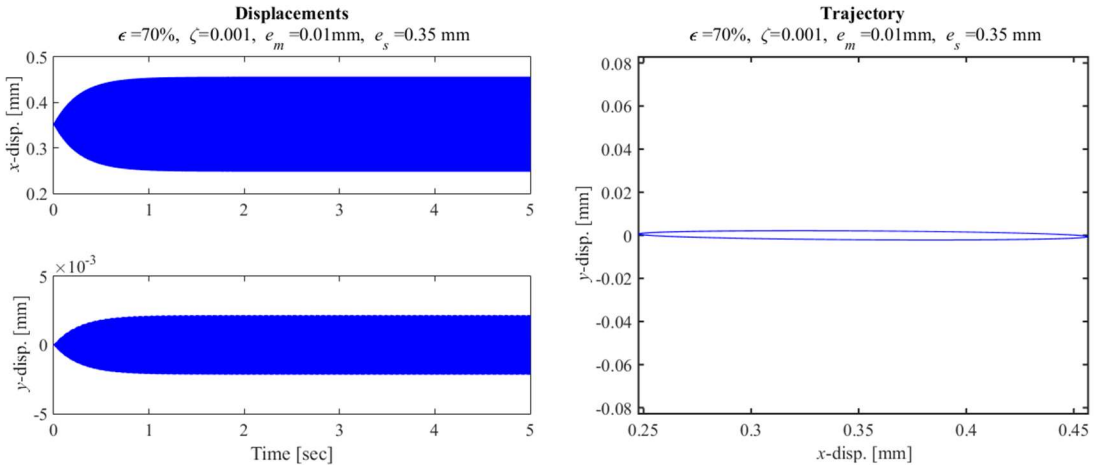

(a) (b)

Figure 53 Rotor system response with the full motor eccentric forces applied. (a) displacements; (b) orbit.

The orbit forms a narrow ellipse with its major axis aligned with the x-axis. This is due to the excitation frequency being nearly equal to the system natural frequency, and the corresponding eccentric motor force harmonic being predominantly along the x axis. The orbit center moved from 0.350 mm to 0.352 mm due to the negative stiffness effect. The vibration amplitude under the full eccentric force effects is 0.1 mm. This is relatively small compared to the motor air gap but may be considered excessive depending on the size of the bearing, seal and other clearances in the machine. Figure 54 shows the displacement spectra of the Jeffcott rotor with 70% eccentricity with the excitation of full eccentric forces.

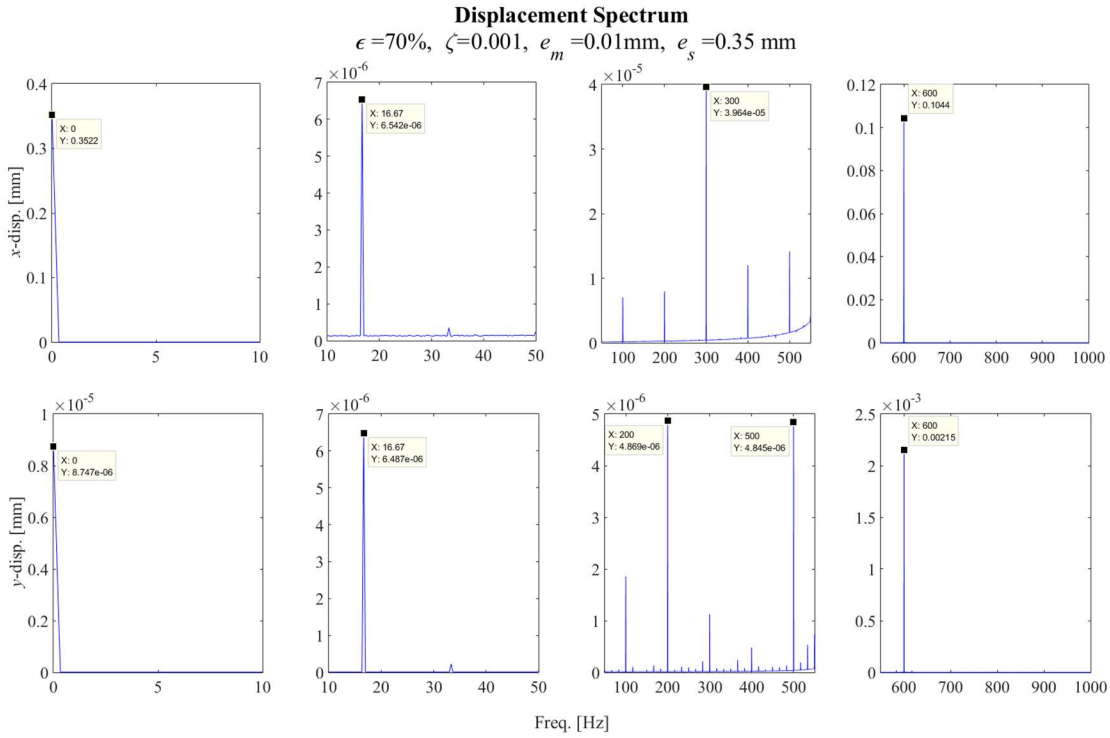

Figure 54 Displacement spectra of the rotor system under the effect of the full motor eccentric force.

The system vibrates about a center near 0.352 mm, which is approximately at 70% motor eccentricity, and has a dominant vibration component at 600 Hz. This is caused by the 600 Hz component in the motor eccentric forces being close to the system natural frequency. Other frequency components at the rotor spin frequency (16.67 Hz) and even multiples of supply frequency $\left(50\times(2N)\text{ Hz},\ N=1,2,3...\right)$ also present as they exist in the excitation forces.

Fig. 59(a) shows the total rotor vibration amplitude plotted vs. motor's static rotor/stator eccentricity (in %), for (a) 0.1% and (b) 0.5% of critical damping applied at the bearings. The vibration amplitude is seen to increase in a nearly linear manner as the motor eccentricity increases, and to decrease inversely proportional to bearing damping.

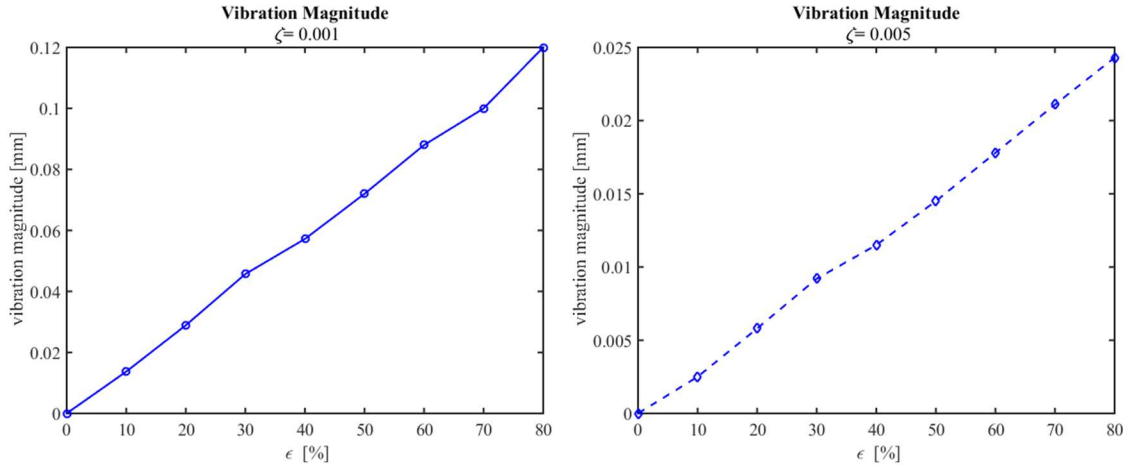

(a) (b)

Figure 55 Rotor center vibration magnitude vs. motor eccentricity for system damping of (a) 0.1% and (b) 0.5%.

Conclusion

This chapter presented a study of the effects of PMSM rotor/stator parallel misalignment (eccentricity) on transverse forces and the resulting vibrations. The eccentricity is shown to produce two important types of transverse force in the forms of a constant component that contributes a negative stiffness and time varying harmonics that could potentially cause resonance if tuned to coincide with a structural natural frequency. Two dimensional (2D) magnetic field simulations were conducted to provide magnetic fields and resulting radial and transverse (to the eccentricity direction) forces as a function of the motor rotor rotation angle. These simulations were performed for sets of eccentricity, current and air gap parameters. The force vs. motor rotor angle arrays were imported into a numerical integration based solution of the system dynamics equations for rotor vibrations, with the zero order force components represented by a negative stiffness, and the time varying component interpolated based on the values in the arrays. The main conclusions reached from the study include:

(1) The radial component of the motor induced transverse force consists of a constant component and harmonics. The frequency of the harmonics occurs at the rotor spin frequency and even multiples of the supply frequency. The dominant harmonic of radial eccentric force occurs at a frequency related to the number of stator coil slots and the number of magnets. The tangential force contains harmonics at the same frequencies as the radial force.

(2) Inclusion of the motor eccentricity produced force harmonics in a vibration simulation may be very important if a potential for resonance exists due to the presence

of natural frequencies with light damping and if eccentric operation might occur due to misalignment of the bearing and motor stator centerlines.

(3) The eccentric forces will cause the orbit of the rotor center to form an elliptical shape in the direction of the eccentricity.

(4) The forces and vibration magnitude increase as the eccentricity increases in almost a linear manner.

(5) Resonant vibrations caused by the eccentric forces can be reduced by adding more damping to the system.

CHAPTER VII

CONCLUSION AND FUTURE WORK

Conclusion

Finite Element Analysis of with Eccentricity

In this dissertation, the finite element analysis of induction motor and permanent magnet synchronous machines, especially with rotor eccentricity, are discussed. A computationally efficient finite element solver modelling motor movements is developed. Field distribution, torque and flux linkage can be obtained by using the finite element solver. The proposed movement modelling method set no limit on the rotor motion thus high accuracy can be maintained without interpolation.

The software is capable of all normal finite element solver functions with focus of force calculation for motor under static eccentricity. The solver can serve as a basic work for future work, allowing further development like efficiency improvement, other eccentricity types (dynamic and mixed eccentricity), other motor types and other motor fault coexistence with eccentricity.

With the aid of this finite element solver, forces experience by the rotor due to eccentricity and their effects on vibration are investigated.

Induction Motor Eccentric Force and Effects on Vibration

Simulated results of induction motor are compared with MEC simulation results from literature, providing an evaluation for MEC simulation prediction of the eccentric

forces. Both radial and tangential force increase nonlinearly with eccentricity and can be represented by a 3rd polynomial function. Stability analysis shows the nonlinear effect of the eccentric force on a Jeffcott rotor model and a geared machinery train. Limit cycle and complex motions are observed due to the nonlinearity of the eccentric force.

PMSM Eccentric Forces and Effects on Vibration

The radial component of the motor induced transverse force consists of a constant component and harmonics. The frequency of the harmonics occur at the rotor spin frequency and even multiples of the supply frequency. The dominant harmonic of radial eccentric force occurs at a frequency related to the number of stator coil slots and the number of magnets. The tangential force contains harmonics at the same frequencies as the radial force. The harmonics of the eccentric force combined with the natural frequency shift caused by the negative stiffness brought by the constant component may cause a system to have large vibration. Resonance might occur.

Future Work

Based on what has been achieved in this research, future works can have the following directions:

Rotordynamic response study of reduced air gap induction motors supported on nonlinear bearing

In the trend of higher performance and more compact design, induction motor with reduced air gap is being used. With a machinery train supported by nonlinear bearings like the film bearings, the nonlinearity that comes from the eccentric force and mechanical support can work to together to have an impact on system stability.

REFERENCES

1. Dorrell, D.G., W.T. Thomson, and S. Roach, Analysis of airgap flux, current, and vibration signals as a function of the combination of static and dynamic airgap eccentricity in 3-phase induction motors. IEEE Transactions on Industry applications, 1997. **33**(1): p. 24-34.
2. Smith, A. and D. Dorrell, Calculation and measurement of unbalanced magnetic pull in cage induction motors with eccentric rotors. I. Analytical model. IEE Proceedings-Electric Power Applications, 1996. **143**(3): p. 193-201.
3. Nandi, S., R.M. Bharadwaj, and H.A. Toliyat. Mixed eccentricity in three phase induction machines: analysis, simulation and experiments. in Industry Applications Conference, 2002. 37th IAS Annual Meeting. Conference Record of the. 2002. IEEE.
4. Wu, L., et al., An analytical model of unbalanced magnetic force in fractional-slot surface-mounted permanent magnet machines. IEEE Transactions on Magnetics, 2010. **46**(7): p. 2686-2700.
5. Mahmoud, H. and N. Bianchi, Eccentricity in synchronous reluctance motors—Part I: Analytical and finite-element models. IEEE Transactions on Energy Conversion, 2015. **30**(2): p. 745-753.
6. Guo, D., F. Chu, and D. Chen, The unbalanced magnetic pull and its effects on vibration in a three-phase generator with eccentric rotor. Journal of sound and Vibration, 2002. **254**(2): p. 297-312.

7. Rahideh, A. and T. Korakianitis, Analytical open-circuit magnetic field distribution of slotless brushless permanent-magnet machines with rotor eccentricity. IEEE Transactions on Magnetics, 2011. **47**(12): p. 4791-4808.
8. Tu, X., et al., Modeling and real-time simulation of internal faults in synchronous generators with parallel-connected windings. IEEE Transactions on Industrial Electronics, 2007. **54**(3): p. 1400-1409.
9. Li, J., Z. Liu, and L. Nay, Effect of radial magnetic forces in permanent magnet motors with rotor eccentricity. IEEE Transactions on magnetics, 2007. **43**(6): p. 2525-2527.
10. Kia, S.H., H. Henao, and G.-A. Capolino, Gear tooth surface damage fault detection using induction machine stator current space vector analysis. IEEE Transactions on industrial Electronics, 2015. **62**(3): p. 1866-1878.
11. Lundin, U. and A. Wolfbrandt, Method for modeling time-dependent nonuniform rotor/stator configurations in electrical machines. IEEE transactions on magnetics, 2009. **45**(7): p. 2976-2980.
12. Donát, M. and D. Dušek, Eccentrically mounted rotor pack and its influence on the vibration and noise of an asynchronous generator. Journal of Sound and Vibration, 2015. **344**: p. 503-516.
13. Tang, Y. and J.A. Kline, Modeling and design optimization of switched reluctance machine by boundary element analysis and simulation. IEEE transactions on energy conversion, 1996. **11**(4): p. 673-680.

14. Li, J., D. Choi, and Y. Cho, Analysis of rotor eccentricity in switched reluctance motor with parallel winding using FEM. IEEE Transactions on Magnetics, 2009. **45**(6): p. 2851-2854.

15. Torkaman, H. and E. Afjei, Hybrid method of obtaining degrees of freedom for radial airgap length in SRM under normal and faulty conditions based on magnetiostatic model. Progress In Electromagnetics Research, 2010. **100**: p. 37-54.

16. Tudorache, T. and I. Trifu, Permanent-magnet synchronous machine cogging torque reduction using a hybrid model. IEEE Transactions on Magnetics, 2012. **48**(10): p. 2627-2632.

17. Werner, U., Rotordynamic model for electromagnetic excitation caused by an eccentric and angular rotor core in an induction motor. Archive of applied mechanics, 2013. **83**(8): p. 1215-1238.

18. Chen, X., S. Yuan, and Z. Peng, Nonlinear vibration for PMSM used in HEV considering mechanical and magnetic coupling effects. Nonlinear Dynamics, 2015. **80**(1-2): p. 541-552.

19. Baoguo, W. and W. Fengxiang. Modeling and analysis of levitation force considering air-gap eccentricity in a bearingless induction motor. in ICEMS'2001. Proceedings of the Fifth International Conference on Electrical Machines and Systems (IEEE Cat. No. 01EX501). 2001. IEEE.

20. Kim, U. and D.K. Lieu, Effects of magnetically induced vibration force in brushless permanent-magnet motors. IEEE Transactions on Magnetics, 2005. **41**(6): p. 2164-2172.

21. Jang, G. and S. Park, Simulation of the electromechanical faults in a single-phase squirrel cage induction motor. IEEE transactions on magnetics, 2003. **39**(5): p. 2618-2620.

22. Xu, X., Q. Han, and F. Chu, Review of electromagnetic vibration in electrical machines. Energies, 2018. **11**(7): p. 1779.

23. Guo, Z., et al., Nonlinear dynamic analysis of rigid rotor supported by gas foil bearings: Effects of gas film and foil structure on subsynchronous vibrations. Mechanical Systems and Signal Processing, 2018. **107**: p. 549-566.

24. Han, X. and A. Palazzolo, Unstable force analysis for induction motor eccentricity. Journal of Sound and Vibration, 2016. **370**: p. 230-258.

25. Li, Y. and A. Palazzolo. PM Synchronous Motor Induced Vibration. in 2018 21st International Conference on Electrical Machines and Systems (ICEMS). 2018. IEEE.

26. Frosini, L. and P. Pennacchi, Detection and modelling of rotor eccentricity in electrical machines: an overview. Vibrations in Rotating Machinery, 2004. **2004**: p. 501-510.

27. Nandi, S., S. Ahmed, and H.A. Toliyat, Detection of rotor slot and other eccentricity related harmonics in a three phase induction motor with different rotor cages. IEEE Transactions on Energy Conversion, 2001. **16**(3): p. 253-260.

28. Nikranjbar, A., M. Ebrahimi, and A.S. Wood, Model-based fault diagnosis of induction motor eccentricity using particle swarm optimization. Proceedings of the Institution of Mechanical Engineers, Part C: Journal of Mechanical Engineering Science, 2009. **223**(3): p. 607-615.

29. Dorrell, D. and A. Smith, Calculation of UMP in induction motors with series or parallel winding connections. IEEE Transactions on Energy Conversion, 1994. **9**(2): p. 304-310.

30. Tabatabaei, I., et al., Modeling and simulation of a salient-pole synchronous generator with dynamic eccentricity using modified winding function theory. IEEE Transactions on Magnetics, 2004. **40**(3): p. 1550-1555.

31. Al-Nuaim, N. and H. Toliyat, A novel method for modeling dynamic air-gap eccentricity in synchronous machines based on modified winding function theory. IEEE Transactions on energy conversion, 1998. **13**(2): p. 156-162.

32. Toliyat, H.A. and N.A. Al-Nuaim, Simulation and detection of dynamic air-gap eccentricity in salient-pole synchronous machines. IEEE transactions on industry applications, 1999. **35**(1): p. 86-93.

33. Faiz, J., et al., Mixed eccentricity fault diagnosis in salient-pole synchronous generator using modified winding function method. Progress In Electromagnetics Research, 2009. **11**: p. 155-172.

34. Zarko, D., et al., Calculation of unbalanced magnetic pull in a salient-pole synchronous generator using finite-element method and measured shaft orbit. IEEE Transactions on Industrial Electronics, 2012. **59**(6): p. 2536-2549.

35. de Canha, D., et al. Methods for diagnosing static eccentricity in a synchronous 2 pole generator. in Power Tech, 2007 IEEE Lausanne. 2007. IEEE.

36. Ebrahimi, B.M., et al., Static eccentricity fault diagnosis in permanent magnet synchronous motor using time stepping finite element method. IEEE Transactions on Magnetics, 2008. **44**(11): p. 4297-4300.

37. Ebrahimi, B.M., J. Faiz, and M.J. Roshtkhari, Static-, dynamic-, and mixed-eccentricity fault diagnoses in permanent-magnet synchronous motors. IEEE Transactions on Industrial Electronics, 2009. **56**(11): p. 4727-4739.

38. Kim, K.-T., et al., Comparison of magnetic forces for IPM and SPM motor with rotor eccentricity. IEEE Transactions on Magnetics, 2001. **37**(5): p. 3448-3451.

39. Ben Yahia, M., et al., Two-Dimensional Exact Subdomain Technique of Switched Reluctance Machines with Sinusoidal Current Excitation. Mathematical and Computational Applications, 2018. **23**(4): p. 59.

40. Zhu, Z., L. Wu, and Z. Xia, An accurate subdomain model for magnetic field computation in slotted surface-mounted permanent-magnet machines. IEEE Transactions on Magnetics, 2010. **46**(4): p. 1100-1115.

41. Tiang, T.L., et al., A comprehensive analytical subdomain model and its field solutions for surface-mounted permanent magnet machines. IEEE Transactions on Magnetics, 2015. **51**(4): p. 1-14.

42. Chen, Z., et al., Modeling and analyzing of surface-mounted permanent-magnet synchronous machines with optimized magnetic pole shape. IEEE Transactions on Magnetics, 2014. **50**(11): p. 1-4.

43. Faiz, J. and M. Ojaghi, Unified winding function approach for dynamic simulation of different kinds of eccentricity faults in cage induction machines. IET electric power applications, 2009. **3**(5): p. 461-470.

44. Faiz, J. and I. Tabatabaei, Extension of winding function theory for nonuniform air gap in electric machinery. IEEE Transactions on Magnetics, 2002. **38**(6): p. 3654-3657.

45. Ghoggal, A., et al. An improved model of the induction machine dedicated to faults detection extension of the modified winding function. in Industrial Technology, 2005. ICIT 2005. IEEE International Conference on. 2005. IEEE.

46. Ghoggal, A., et al. A winding function-based model of air-gap eccentricity in saturated induction motors. in Electrical Machines (ICEM), 2012 XXth International Conference on. 2012. IEEE.

47. Alam, F.R. and K. Abbaszadeh, Magnetic field analysis in eccentric surface-mounted permanent-magnet motors using an improved conformal mapping method. IEEE Transactions on Energy Conversion, 2016. **31**(1): p. 333-344.

48. Ostovic, V., A method for evaluation of transient and steady state performance in saturated squirrel cage induction machines. IEEE Transactions on Energy Conversion, 1986(3): p. 190-197.

49. Ostović, V., Magnetic equivalent circuit presentation of electric machines. ELECTRIC MACHINES AND ELECTROMECHANICS, 1987. **12**(6): p. 407-432.

50. Ostovic, V., A simplified approach to magnetic equivalent-circuit modeling of induction machines. IEEE Transactions on Industry Applications, 1988. **24**(2): p. 308-316.

51. Ostovic, V., A novel method for evaluation of transient states in saturated electric machines. IEEE Transactions on Industry Applications, 1989. **25**(1): p. 96-100.

52. Zhang, M., et al. Magnetic equivalent circuit modeling for interior permanent magnet synchronous machine under eccentricity fault. in Power Engineering Conference (UPEC), 2013 48th International Universities'. 2013. IEEE.

53. Hong, J., et al., Detection and classification of rotor demagnetization and eccentricity faults for PM synchronous motors. IEEE Transactions on Industry Applications, 2012. **48**(3): p. 923-932.

54. Salon, S.J., Finite element analysis of electrical machines. Vol. 101. 1995: Kluwer academic publishers Boston USA.

55. Bastos, J.P.A. and N. Sadowski, Electromagnetic modeling by finite element methods. 2003: CRC press.

56. Ling, Z., et al., Equivalent circuit parameters calculation of induction motor by finite element analysis. IEEE Transactions on Magnetics, 2014. **50**(2): p. 833-836.

57. Zhong, D., Finite element analysis of synchronous machines. 2009.

58. Thomas, A., Z. Zhu, and L. Wu, Novel modular-rotor switched-flux permanent magnet machines. IEEE Transactions on Industry Applications, 2012. **48**(6): p. 2249-2258.

59. Kim, M.-J., et al., Analysis of inverter-fed squirrel-cage induction motor during eccentric rotor motion using FEM. IEEE Transactions on Magnetics, 2008. **44**(6): p. 1538-1541.

60. Faiz, J., et al., Finite-element transient analysis of induction motors under mixed eccentricity fault. IEEE transactions on magnetics, 2008. **44**(1): p. 66-74.

61. Vandevelde, L., J.J. Gyselinck, and J.A. Melkebeek, Long-range magnetic force and deformation calculation using the 2D finite element method. IEEE transactions on magnetics, 1998. **34**(5): p. 3540-3543.

62. Thomson, W.T. and A. Barbour, On-line current monitoring and application of a finite element method to predict the level of static airgap eccentricity in three-phase induction motors. IEEE Transactions on Energy Conversion, 1998. **13**(4): p. 347-357.

63. Faiz, J., et al., Comprehensive eccentricity fault diagnosis in induction motors using finite element method. IEEE Transactions on Magnetics, 2009. **45**(3): p. 1764-1767.

64. He, G., et al., Numerical prediction of electromagnetic vibration and noise of permanent-magnet direct current commutator motors with rotor eccentricities and glue effects. IEEE Transactions on Magnetics, 2012. **48**(5): p. 1924-1931.

65. Li, J., et al., Effects of MMF harmonics on rotor eddy-current losses for inner-rotor fractional slot axial flux permanent magnet synchronous machines. IEEE Transactions on Magnetics, 2012. **48**(2): p. 839-842.

66. Pennacchi, P. and L. Frosini, Dynamical behaviour of a three-phase generator due to unbalanced magnetic pull. IEE Proceedings-Electric Power Applications, 2005. **152**(6): p. 1389-1400.

67. Lipo, T.A., Introduction to AC machine design. Vol. 63. 2017: John Wiley & Sons.

68. Han, X., Discussion of Induction Motor Effect on Rotordynamics. 2015.